

BALLISTIC TRANSPORT AND LARGE SPIN HALL EFFECT IN A SILICENE MOSFET

A Thesis

Presented to the Faculty of the Graduate School
of Cornell University

in Partial Fulfillment of the Requirements for the Degree of
Master of Science

by

Maxwell N. Fishman

January 2017

© 2017 Maxwell N. Fishman
ALL RIGHTS RESERVED

ABSTRACT

In an effort to surmount the issues that arise when attempting to scale transistors down to the low nanometer regime, the use of two-dimensional materials in transistors is regarded as a possible solution. One such material, silicene, has garnered much attention recently due to its unique properties and compatibility with current silicon-based technology. Silicene is a silicon analog of graphene in which a monolayer of silicon atoms forms a honeycomb structure. Therefore, silicene contains many of the properties of graphene. However, due to its buckled structure and larger spin orbit coupling, silicene has a gapped band structure. Moreover, application of an electric field perpendicular to the silicene plane has been shown to induce band splitting and band gap manipulation.

In this thesis, the reported electronic and topological properties of silicene are investigated using a low-energy effective Hamiltonian. It is confirmed that silicene's band structure is strongly manipulated by the application of a vertical electric field. Furthermore, by calculation of the Z_2 topological invariant, it is confirmed that when the electric field surpasses a critical value silicene transitions from topological insulator to band insulator. The use of silicene in a ballistic independent double gate field effect transistor is also modeled. It is found that while the drain current exhibits the current saturation expected of a field effect transistor, the use of asymmetric gate voltages generates a transverse spin current perpendicular to the drain current. The spin current is found to have a switching capability, depending on whether the vertical electric field generated by the asymmetric gate voltages is greater than or less than a critical value. This property is very interesting and could have spintronic applications.

BIOGRAPHICAL SKETCH

Maxwell Fishman earned his Bachelor of Science degree in Mechanical Engineering from Rutgers University in 2012. After earning his Bachelor's degree, he worked as a mechanical engineer at Structured Materials Industries, Inc. in Piscataway, New Jersey. During his time at Structured Materials Industries, Inc., Maxwell worked as a system designer of chemical vapor deposition systems.

After leaving Structured Materials Industries, Inc. in order to pursue a graduate degree, Maxwell joined the Master of Science program at Cornell University. Maxwell's thesis entitled "Ballistic Transport and Large Spin Hall Effect in a Silicene MOSFET" was supervised by Dr. Debdeep Jena.

ACKNOWLEDGEMENTS

It is an honor and a privilege to thank those who helped and supported me in my academic efforts that ultimately lead to the writing of this thesis.

Firstly, I thank Professor Debdeep Jena for being a wonderful advisor and mentor. Without his guidance and insight this thesis would not have been possible. Furthermore, I thank him for his patience in discussing my myriad of research questions and taking the time to explain concepts in a clear and intuitive manner. I also thank the Jena-Xing group whose compelling research and inspiring work ethic greatly spurred my own research efforts.

I thank Professor David Muller, my second committee member and director of the applied physics master's program, for his advise and support during my time in the Master of Science program.

Lastly, I thank my parents. None of this would have been possible without their support and encouragement.

TABLE OF CONTENTS

Biographical Sketch	iii
Acknowledgements	iv
Table of Contents	v
List of Figures	vi
1 Introduction and Motivation	1
2 Theoretical Background	3
2.1 Graphene: Entry Point for 2D Materials	3
2.2 Silicene: Graphene Plus Buckling	6
2.3 Berry Curvature and Anomalous Velocity	8
2.4 Topological Insulators and the Quantum Spin Hall Effect	10
2.5 Ballistic Transport	13
3 Silicene Electronic Properties	18
3.1 Band Structure of Silicene	18
3.2 Density of States	22
3.3 Berry Curvature	25
3.4 Z_2 Topological Invariant	28
3.5 Electron Velocity	30
4 Silicene 2D FET Modeling & Results	35
4.1 Carrier Density	35
4.2 Conventional Source-Drain Current	40
4.3 Transverse Current	45
5 Conclusions & Future Prospects	51
A Electron Velocity Profiles	53
B Transverse Electron Current	56
Bibliography	57

LIST OF FIGURES

2.1	a) Graphene primitive lattice and basis. b) Graphene reciprocal lattice and first Brillouin zone	3
2.2	a) Graphene tight-binding energy dispersion. b) Low-energy linear dispersion.	5
2.3	Silicene lattice in a) XY plane and b) XZ plane.	7
2.4	Graphical representation of a) QSH spin polarized edge transport, which are protected against scatterers, and b) QSH band structure. Red and blue represent different spin states.	11
2.5	a) Sketch of a double gate 2D FET device. b) Band diagram without the application of a drain voltage bias. c) Sketch of Fermi circle without applied drain bias.	14
2.6	a) General band diagram of a FET in the source-drain direction with applied bias V_{ds} . b) Sketch of Fermi circle when bias is applied.	15
2.7	General band diagram of a double gate 2D FET in the direction of the gate-insulator-channel (chosen to be z-axis)	17
3.1	Action of the nearest neighbor creation/annihilation operators on the silicene lattice.	19
3.2	Silicene low-energy band structure at a) $E_z = 0$, b) $E_z < E_c$, and c) $E_z = E_c$, and d) $E_z > E_c$. Arrows indicate spin.	21
3.3	Total DOS at a) $E_z = 0$, b) $ E_z < E_c $, c) $ E_z = E_c $, and d) $ E_z > E_c $	24
3.4	Spin up (blue) and spin down (red) conduction band Berry curvature near K_+ at a) $E_z = 0$, b) $E_z < E_c$, c) $E_z > E_c$, and d) $E_z \gg E_c$	26
3.5	Spin up (blue) and spin down (red) conduction band Berry curvature near K_- at a) $E_z = 0$, b) $E_z < E_c$, c) $E_z > E_c$, and d) $E_z \gg E_c$	27
3.6	Partial Chern numbers for a) spin up states near K_+ , b) spin up states near K_- , c) spin down states near K_+ , and d) spin down states near K_-	29
3.7	Spin chern number difference, n_σ , versus perpendicular electric field	30
3.8	Spin up conduction band velocity profile near K_+ Dirac point at a) $E_z = 0$, b) $E_z < E_c$, $E_z > E_c$, and d) $E_z \gg E_c$. The length of the arrows are proportional to the magnitude of the velocities.	32
3.9	Spin up conduction band velocity profile of standard (red) and Berry (blue) velocities near K_+ Dirac point at a) $k_x = k_y = 5 \times 10^{-3} \text{ nm}^{-1}$, and b) $k_x = k_y = 2 \times 10^{-3} \text{ nm}^{-1}$	33
4.1	(a) charge, (b) field, and (c) band diagram of a general 2D independent double gate FET in the gate-channel-gate direction	36
4.2	Carrier density at 300K and $V_{gs,TG} = V_{gs,BG}$ (red) and $V_{gs,BG} = 0$ (blue)	39

4.3	Carrier density at 300K and $V_{gs,TG} = V_{gs,BG} = 0$ V (red) and $V_{gs,TG} = V_{gs,BG} = 0.2$ V (blue)	40
4.4	Current density at 300K and $V_{gs,TG} = V_{gs,BG} = 0$ V (red), $V_{gs,TG} = V_{gs,BG} = 0.2$ V (blue), and $V_{gs,TG} = 0.2$ V, $V_{gs,BG} = 0$ V (green)	42
4.5	Current density at 300K and $V_{ds} = 0.1$ V (red) and $V_{ds} = 0.2$ V (blue) with symmetric gate voltages	42
4.6	Current density at 300K and a) $E_f = 0.1$ eV and b) $n_s = 5 \times 10^{12} \text{ cm}^{-2}$	43
4.7	Current density at 300K (solid) and 50K (dashed) at $V_{ds} = 0.2$ V for electron transport (blue), hole transport (red), and total transport (green). Symmetric gate voltages are used.	44
4.8	I_{ON}/I_{OFF} ratio at $V_{ds} = 0.2$ V, $V_{gs,TG}^{ON} = V_{gs,BG}^{ON} = 0.1$ V (blue), and $V_{gs,TG}^{ON} = V_{gs,BG}^{ON} = 0.2$ V (red).	45
4.9	Transverse current density at 300K and $E_z = -5$ (red), $E_z = -20$ (blue), $E_z = 5$ (green), and $E_z = 20$ (orange). The left plot (a) is the current for spin up states near K_+ and the right plot (b) is the total spin current over all conduction bands. E_z in mV/Å.	47
4.10	Total transverse spin current density at 300K at a) $E_f = 0$ eV (red) and $E_f = 0.1$ eV (blue) and b) $n_s = 5 \times 10^{12} \text{ cm}^{-2}$	48
4.11	Transverse spin current density at 300K due to conduction and valence band transport. (a) Conduction (red) and valence (blue) band current densities at $E_z = 0$ (solid) and $E_z = 20$ (dashed). (b) Total current density at $E_z = 0$ (red), $E_z = 10$ (blue), $E_z = 20$ (green), and $E_z = 30$ (orange). E_z in mV/Å.	49
4.12	Spin current ratio at 300K, $V_{ds} = 0.1$ V, and $L_{ch} = 10$ nm. (a) Total spin current density at $E_z = 0$ mV/Å (red) and $E_z = 20$ mV/Å (blue). (b) Corresponding spin current ratios.	50
A.1	Spin down conduction band velocity profile near K_+ Dirac point at a) $E_z = 0$, b) $E_z < E_c$, $E_z > E_c$, and d) $E_z \gg E_c$. The length of the arrows are proportional to the magnitude of the velocities.	53
A.2	Spin up conduction band velocity profile near K_- Dirac point at a) $E_z = 0$, b) $E_z < E_c$, $E_z > E_c$, and d) $E_z \gg E_c$. The length of the arrows are proportional to the magnitude of the velocities.	54
A.3	Spin down conduction band velocity profile near K_- Dirac point at a) $E_z = 0$, b) $E_z < E_c$, $E_z > E_c$, and d) $E_z \gg E_c$. The length of the arrows are proportional to the magnitude of the velocities.	55
B.1	Transverse spin current at 300K and $E_z = -5$ (red), $E_z = -20$ (blue), $E_z = 5$ (green), and $E_z = 20$ (orange). E_z in mV/Å.	56

CHAPTER 1

INTRODUCTION AND MOTIVATION

Since the first transistor was created in 1947 [1], semiconductor devices have been steadily decreasing in size at a rate comparable to that predicted by Moore's Law. This decrement in size has lead to large improvements in device performance and efficiency. However, devices are now reaching near atomic scale lengths and this creates numerous hurdles which prevent further size reduction. The latest transistors have gate lengths in the low nanometer regime and at this scale the probability of electrons tunneling from the source to the drain becomes problematic. This has lead to novel devices that make use of tunneling, but there are still many other issues that arise when devices reach these lengths. As the size of a 3D semiconductor is reduced to the nanometer scale and below, the band gap of the material begins to rapidly increase due to quantum confinement. Also, as the material size decreases, the effects of surface states due to dangling bonds and surface roughness become much greater. In the nanometer scale, these issues cause a great impediment to creating 3D devices [2].

In an effort to overcome the aforementioned hurdles when using 3D materials, a great deal of investigation is being done into the use of 2D materials in devices. Many of the issues that prevent further size reduction in 3D materials are resolved in 2D materials. The inherently thin nature of 2D materials makes them more robust against the effects of quantum confinement. Also, 2D materials do not have the dangling bond and surface roughness issues that cause problems in 3D materials. Many 2D materials also have unique properties, such as a linear band structure, that make them particularly exciting for new device

research. The use of 2D materials in devices will potentially lead to smaller scale devices.

As one of the oldest and most researched 2D materials, graphene has many unique properties that would make it very useful in devices. However, due to the gapless band structure of graphene, preventing current leakage in devices is difficult. Therefore, there is a great deal of research into materials that retain many of the properties of graphene, but also have a notable band gap. One such material that has received attention recently is silicene. Silicene can be considered a silicon analog of graphene and has many of the properties of graphene as well as numerous unique properties. Unlike graphene, which is completely planar, silicene has a buckled structure. Due to this structure, application of an electrical field perpendicular to the material plane can alter the electronic properties of silicene and also cause topological phase changes.

In this thesis, the electronic and topological properties of silicene are examined under various electric field strengths. Furthermore, ballistic transport of a silicene field effect transistor (FET) is modeled and analyzed. In chapter 2, a brief theoretical background of silicene and ballistic transport is given. Using this background, the electronic and topological properties of silicene are analyzed in chapter 3. In chapter 4, the ballistic transport model derivation and results of a silicene FET are discussed. Finally, in chapter 5, the conclusions are summarized and future prospects discussed.

CHAPTER 2

THEORETICAL BACKGROUND

2.1 Graphene: Entry Point for 2D Materials

Graphene is one of the most well researched 2D materials. Thus, graphene often serves as the foundation for research into more exotic 2D materials. This is due to the atomic structure and properties of many 2D materials being very similar to that of graphene. With this in mind, it is prudent to begin with an introduction to graphene, as it will allow for easier understanding of the unique properties of silicene.

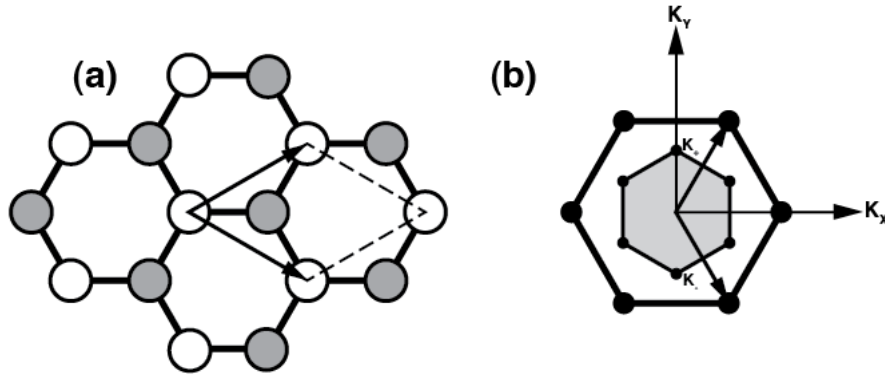


Figure 2.1: a) Graphene primitive lattice and basis. b) Graphene reciprocal lattice and first Brillouin zone

Graphene is a 2D allotrope of carbon which has received immense experimental attention ever since stable monolayers were created in 2004 [3],[4]. Graphene has a honeycomb structure, which can be described as a hexagonal Bravais lattice with a two atom basis (figure 2.1a). Since graphene is completely planar and carbon has four valence electrons, the carbon atoms are bonded to each other through sp^2 bonding. The p_z (arbitrarily chosen to be the orbital

perpendicular to the sheet plane) orbitals, which do not interact with the sp^2 orbitals, contain one electron per carbon atom and form π bond with each other [4, 5]. It should be noted that in actuality there are interactions between the p_z orbitals and the sp^2 orbitals, however these interactions are minimal and can often be neglected.

As previously stated, to a good approximation the p_z orbitals can be considered to be completely uncoupled from all other orbitals in graphene. Since these orbitals contain only one electron per atom, it is clear that the electronic properties of graphene will result from the interactions between the p_z orbitals. Using a tight binding analysis with the p_z orbitals and nearest-neighbor interactions, one finds the band structure to be [4, 6]

$$E_{\pm} = \pm \sqrt{t^2 \left[1 + 4 \cos\left(\frac{3}{2}k_x a\right) \cos\left(\frac{\sqrt{3}}{2}k_y a\right) + 4 \cos^2\left(\frac{\sqrt{3}}{2}k_y a\right) \right]}, \quad (2.1)$$

where \pm refers to the conduction (+) and valence (−) bands, the on-site energies of the two carbon atoms in each unit cell (figure 2.1a) are defined to be zero, k_x and k_y are wave vectors in momentum space (figure 2.1b), $t = 3.0$ eV is the hopping energy, and $a = 0.15$ nm is the distance between the two basis atoms. A graphical view of equation 2.1 can be seen in figure 2.2. At low energies, the band becomes conical and the energy gaps close at the corners of the first Brillouin zone (FBZ) (figure 2.1b). These FBZ corners are often referred as the Dirac points. Considering that most of the applications of graphene are relatively low energy, it is useful to expand equation 2.1 about a Dirac point. In doing so, one finds

$$E_{\pm} = \pm \hbar v_f \sqrt{k_x^2 + k_y^2}, \quad (2.2)$$

where k_x and k_y are now measured relative to the Dirac point and the “Fermi”

velocity is

$$v_f = \frac{\sqrt{3}at}{2\hbar} \approx 10^8 \text{ cm/s.} \quad (2.3)$$

To a first order approximation, the band structure is completely conical and gapless at the Dirac points (figure 2.2). At low energies, the second and higher order terms of the energy dispersion (equation 2.1) are negligible. This linear band structure is one of the unique properties of graphene that drives research into this material. Graphene has numerous other unique properties as well, such as pseudospin chirality, Klein tunneling, and the quantum hall state, but these will not be covered in this thesis. If the reader is interested, references [3] and [4] are suggested.

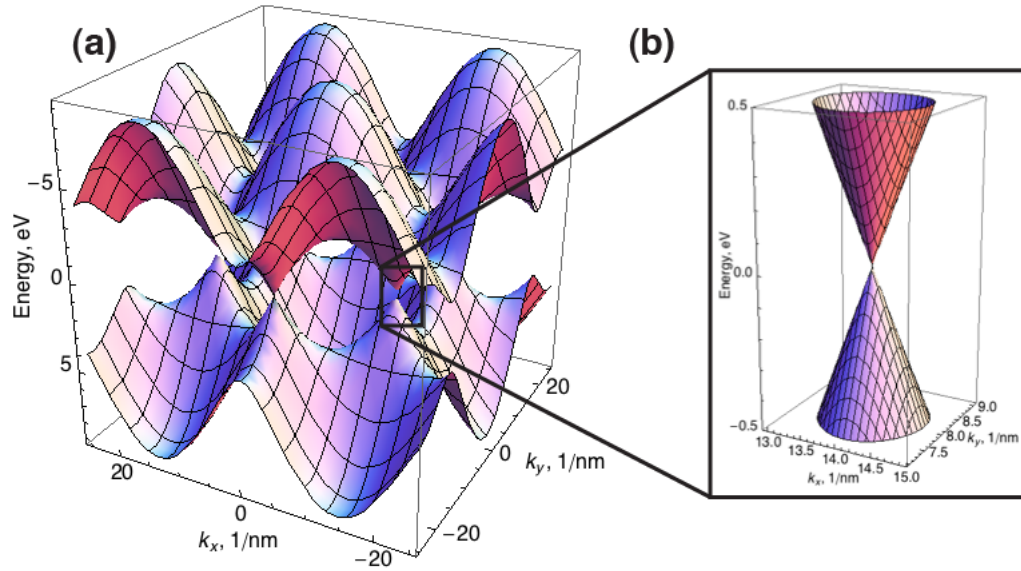


Figure 2.2: a) Graphene tight-binding energy dispersion. b) Low-energy linear dispersion.

Although the linear energy dispersion makes graphene a very interesting material, the gapless band structure of graphene makes utilization in transistors difficult. A basic requirement of transistor switch is a sharp on and off state, but since graphene has a gapless band structure it is always readily con-

ductive regardless of Fermi level and temperature. Therefore, to prevent major off state current leakage in transistor switches, finding a suitable method to incorporate a band gap into graphene is of great interest. This research includes bilayer graphene [7], transition metal dichalcogenides [8], and recently silicene has gained interest [9].

2.2 Silicene: Graphene Plus Buckling

As mentioned in the previous section, one of the newer and more exotic 2D materials that is being considered as a graphene-like material that contains a notable band gap is a silicon analog of graphene called silicene. Silicene has the same honeycomb structure as graphene, but the basis atoms are silicon instead of carbon. Until recently, silicene was primarily considered a theoretical material since monolayers of silicon were found to rapidly decompose in air, making growth of stable silicene very difficult. However, recent advances in silicene growth techniques show the potential for this material to be used in devices [10].

In the previous section, spin orbit coupling was not considered in the tight binding analysis of graphene. It is acceptable to neglect spin orbit coupling (SOC) in graphene, because these interactions are very weak and only make notable contributions in extreme conditions. This weak SOC can be attributed to the size of the graphene atoms and the spatial inversion symmetry that is found in graphene. However, the larger silicon atoms in silicene cause it to have a very unique buckled structure, which can be seen in figure 2.3. The larger size of the silicon atoms as well as the buckled structure cause silicene to have a

larger SOC than graphene. This SOC opens up a notable band gap in silicene. It should be noted that although silicene has a larger SOC than graphene, the SOC in silicene is still small relative to heavier elements (lower on the periodic table). As a point of comparison, density functional theory calculations predict a SOC band gap of approximately 1.55 meV in silicene, approximately 24 μeV in graphene, and a spin split-off band gap of 0.8 eV in InSb [9, 11, 12].

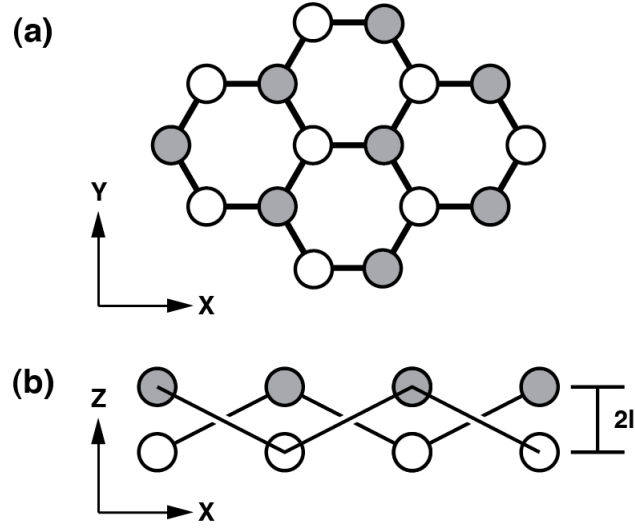


Figure 2.3: Silicene lattice in a) XY plane and b) XZ plane.

As shown in figure 2.3, the buckled structure of silicene creates two planes of atoms. Each plane is composed of one of the two basis atoms. When an electric field is applied perpendicular to these planes, it is clear that a potential difference will occur between the planes and this difference will modify silicene's Hamiltonian. Therefore, one can use a perpendicular electric field to modify the band structure of silicene [9]. A quantitative analysis of how a perpendicular electric field effects silicene's band structure will be carried out in the next chapter.

Since one can modify the band structure of silicene using an electric field, it

has been predicted that sweeping the electric field strength to cause the band gap of silicene to close and re-open results in a phase change from a topological insulator to a band insulator [9, 13]. An introduction to topological insulators will be given in section 2.4.

2.3 Berry Curvature and Anomalous Velocity

As mentioned in the previous section, the breaking of spatial inversion symmetry in silicene by its buckled structure results in very unique properties. Another interesting property that is likely to arise from this broken symmetry is a non-trivial Berry curvature that has different values at different valleys (Dirac points in silicene and graphene). Therefore, in this section the concept of Berry phase and Berry curvature will be introduced and the latter will be shown to lead to remarkable transport properties.

The core concept behind the Berry phase stems from the phase factor that is acquired when a system is adiabatically swept through the parameter space that describes the system. Sweeping adiabatically is required, since this causes the system to always remain in the same instantaneous eigenstate throughout the whole process. Therefore, in this scheme the phase factor can be isolated since it is the only degree of freedom and the phase factor is found to be

$$\gamma_n = \int_C d\mathbf{R} \cdot \mathbf{A}_n(\mathbf{R}), \quad (2.4)$$

where

$$\mathbf{A}_n(\mathbf{R}) = i\langle n(\mathbf{R}) | \frac{\partial}{\partial \mathbf{R}} | n(\mathbf{R}) \rangle, \quad (2.5)$$

where \mathbf{R} is a generalized parameter space (in the regime of solid state physics

this is usually taken to be momentum space), $|n(\mathbf{R})\rangle$ is the eigenstate of the n th band at \mathbf{R} , and $A(\mathbf{R})$ is referred to as the Berry connection or Berry potential [14].

Therefore, it is found that this phase factor solely depends on the path taken in parameter space. For this reason, it is often referred to as the geometric phase. This phase factor is gauge dependent and by using the appropriate gauge the phase can always be eliminated. The only situation in which the phase factor becomes gauge independent is when the system is cyclically swept through the parameter space on a closed path. This was first discovered by Sir Michael Berry in 1984, hence the name Berry phase [15].

Using Stokes' theorem, the Berry phase can be recast as

$$\gamma_n = \int_S d\mathbf{S} \cdot \boldsymbol{\Omega}_n(\mathbf{R}), \quad (2.6)$$

$$\boldsymbol{\Omega}_n = \nabla_{\mathbf{R}} \times \mathbf{A}_n(\mathbf{R}), \quad (2.7)$$

where $\boldsymbol{\Omega}_n$ is referred to as the Berry curvature. It should be noted that equation 2.7 assumes a three dimensional parameter space. The Berry curvature can be generalized to higher dimensions, however for most purposes of interest the parameter space is three dimensional momentum space. Furthermore, equation 2.7 can be written as the following

$$\Omega_{\mu\nu}^n(\mathbf{R}) = i \sum_{n \neq n'} \frac{\langle n | \partial H / \partial R^\mu | n' \rangle \langle n' | \partial H / \partial R^\nu | n \rangle - \langle n | \partial H / \partial R^\nu | n' \rangle \langle n' | \partial H / \partial R^\mu | n \rangle}{(\varepsilon_n - \varepsilon_{n'})^2}, \quad (2.8)$$

in which H is the Hamiltonian, $R^{\mu(\nu)}$ is the μ th (ν th) component of \mathbf{R} , and ε_n is the energy dispersion of the n th band. This is merely a summation over eigenstates. In this thesis, equation 2.7 is used to check the results of equation 2.8. Since equation 2.8 is found to be less computationally intensive, it is the primary method used for calculating Berry curvature.

At first glance the Berry curvature may seem like a trivial expansion on

the Berry connection. However, since the Berry curvature is gauge invariant it should be observable. The Berry connection will not be observable, because it is not gauge invariant. One way in which Berry curvature can be observed is through the effect it has on electron dynamics in condensed matter systems. It has recently been found that in the presence of an electric field, the electron group velocity acquires an extra component that is proportional to the Berry curvature of the band. Therefore, the full expression for electron velocity in the presence of an electric field becomes [14]

$$\mathbf{v}_n(\mathbf{k}) = \frac{\partial \varepsilon_n(\mathbf{k})}{\hbar \partial \mathbf{k}} - \frac{e}{\hbar} \mathbf{E} \times \boldsymbol{\Omega}_n(\mathbf{k}), \quad (2.9)$$

where the first term on the right hand side is the standard quantum mechanical electron group velocity and the second term is the additional "anomalous" velocity due to Berry curvature. As we will see in subsequent chapters, this anomalous velocity leads to very interesting and unique transport properties in materials with non-trivial Berry curvatures.

2.4 Topological Insulators and the Quantum Spin Hall Effect

Condensed matter physics in large part has been the study of how symmetry breaking leads to unique states of matter. For instance, crystalline solids result from a breaking of continuous translation and rotation symmetries. However, states of matter have recently been discovered that can not be uniquely described in terms of broken symmetries. This has led to a new paradigm for describing these states of matter, known as topological order. Although the quantum hall state was the first state of matter discovered that could not be appropriately described in terms of symmetry breaking, this thesis will focus on

a more recent state of matter known as the quantum spin hall (QSH) state. For a comprehensive description of the quantum hall state, references [16] and [17] are suggested.

Adapted from mathematical topology, it was found that band structures could be classified according to topological invariants. These topological classes describe all equivalent Hamiltonians that can be smoothly deformed into each other without closing the band gap. If a change in the system properties causes the band gap to close and re-open then a non-smooth change in the Hamiltonian has taken place and this is a strong indicator of a topological phase change [18]. The invariant that describes these equivalent classes of Hamiltonians is known as the Chern invariant and is found by integrating the Berry curvature,

$$n_m = \frac{1}{2\pi} \int_{FBZ} d^2\mathbf{k} \Omega_m(\mathbf{k}), \quad (2.10)$$

where n_m and Ω_m are the Chern number and Berry curvature for the m th band. Summing the Chern number over all occupied bands is the Chern invariant. This invariant is always an integer and is directly related to the genus in the Gauss-Bonnet theorem of two dimensional surface topology [18]. For reference, the Chern invariant for band insulators is 0 and 1 for the quantum hall state.

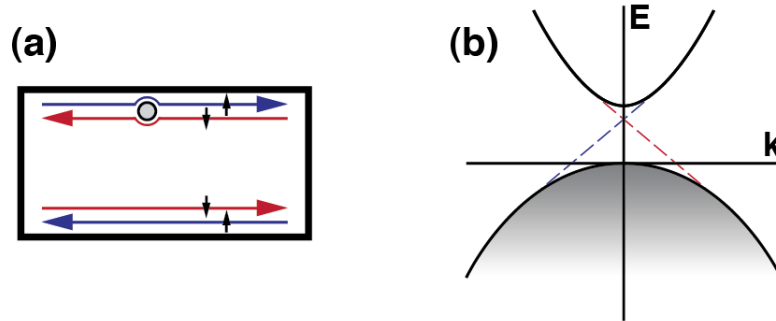


Figure 2.4: Graphical representation of a) QSH spin polarized edge transport, which are protected against scatterers, and b) QSH band structure. Red and blue represent different spin states.

Although the Chern invariant succeeds in uniquely classifying different topological phases of matter, recently a new phase of matter has been discovered for which the Chern invariant is inadequate. The QSH state (often referred to as a topological insulator), was first predicted in 2005 by Kane and Mele [19] and experimentally observed in 2007 by König in HgTe quantum wells [20]. The topological insulator is characterized by having a gapped insulator band structure in the bulk, but also having spin polarized gapless edge states as illustrated in figure 2.4a. A representation of this band structure can be seen in figure 2.4b. Since the edge states are spin polarized, they are robust against scattering from non-magnetic defects (figure 2.4a). Furthermore, unlike the quantum hall state, an external magnetic field is generally not required to create a QSH state. This gives topological insulators a great deal of potential for uses in devices that require spin control and low energy dissipation, such as spintronics and quantum computation [21, 22].

Unlike the quantum hall state, topological insulators do not have a unique Chern invariant. If one were to calculate this invariant, the result would be the same as that of a band insulator. This is due to the fact that topological insulators generally preserve time reversal symmetry [23]. Therefore, an additional topological invariant, referred to as the Z_2 invariant, distinguishes between band insulator and topological insulator. Calculating the Z_2 invariant from band structure can be cumbersome, but if the system conserves spin s_z then the formulations are greatly simplified by the use of spin Chern numbers [24]. Under this paradigm, the Z_2 invariant is found to be

$$\nu = n_\sigma \bmod 2 \tag{2.11}$$

$$n_\sigma = (n_\uparrow - n_\downarrow)/2 \tag{2.12}$$

where ν is the Z_2 invariant and n_σ is the spin Chern number difference. Since this thesis theoretically analyzes silicene, it is assumed to be without disorder and s_z is indeed conserved.

As previously mentioned, it is usually the case that a topological phase change results from adjusting a property of the system that modifies the Hamiltonian in a non-smooth manner. This change should subsequently cause the band gap to shrink to zero and then re-open. For instance, in the first experiments in which the QSH effect was observed, the adjusted property was the well thickness in HgTe quantum wells. Once the well width is increased beyond a critical value (~ 6.3 nm) spin polarized edge states developed, indicating a change from band insulator to topological insulator [20, 25].

As with the work done on HgTe quantum wells, it is claimed that silicene also undergoes a phase change when a property is swept through a critical value. However, in the case of silicene the property is the strength of an electric field applied perpendicularly to the silicene layer. Due to the strong SOC and the buckled nature of silicene, it is expected that silicene is intrinsically a topological insulator and if an electric field is applied that is beyond a critical strength value (~ 17 mV/Å) it changes to a band insulator. In this thesis, the calculated berry curvature of silicene is used to find the Z_2 invariant and confirm the topological order.

2.5 Ballistic Transport

As mentioned in chapter 1, the purpose of this thesis is not only to analyze the topological properties of free-standing silicene, but to also examine how

these unique properties influence transport in devices. In particular, this thesis will examine the transport properties of silicene in a independent double-gated FET (IDGFET) scheme. As devices shrink in size, electron scattering is reduced and the transport properties approach the ballistic regime. With this in mind, the ideal ballistic case will be the focus of this device model. This section will highlight the physics of ballistic transport. For a more comprehensive study of ballistic transport, the reader is referred to [26, 27].

Starting with a simple case, the IDGFET device is initially considered with zero bias on both gates. A sketch of such a device is shown in figure 2.5a and is composed of a source, drain, a semiconducting channel material between the two, and a gate-insulator combination above and below the channel. For this thesis, the semiconducting device will be silicene, but this model applies to any material with any band structure. Therefore, in this section the model will be described in a general sense. Application of this model to the specific case of silicene will take place in the next chapter.

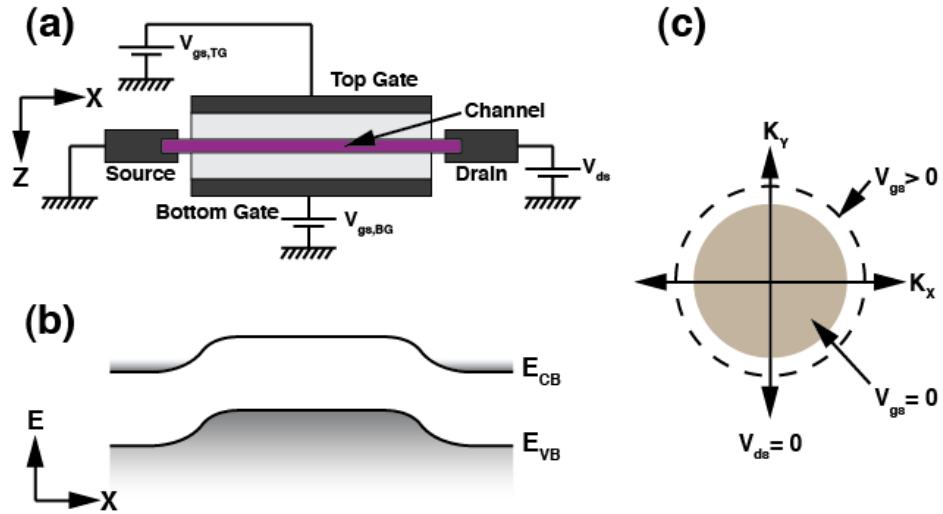


Figure 2.5: a) Sketch of a double gate 2D FET device. b) Band diagram without the application of a drain voltage bias. c) Sketch of Fermi circle without applied drain bias.

If one assumes that the source and drain are the same material and their Fermi level is equal to the conduction band of the semiconductor material, the band diagram will look like that shown in figure 2.5b. Application of a voltage bias between the source and drain causes the picture to shift to that shown in figure 2.6a. The source-drain current can be considered as a summation of left-going and right-going currents. Without a bias, these two currents are equal and opposite, generating a total current of zero. With a positive drain voltage, amount of carriers moving in the source-drain direction are increased and carriers in the drain-source direction are decreased. This concept should be clear if one considers how a general Fermi-circle is altered when a voltage difference is applied. A sketch of this is shown in figure 2.6b. Therefore, the total carrier density is always constant and the source-drain bias merely modifies the ratio of right-going to left-going carriers.

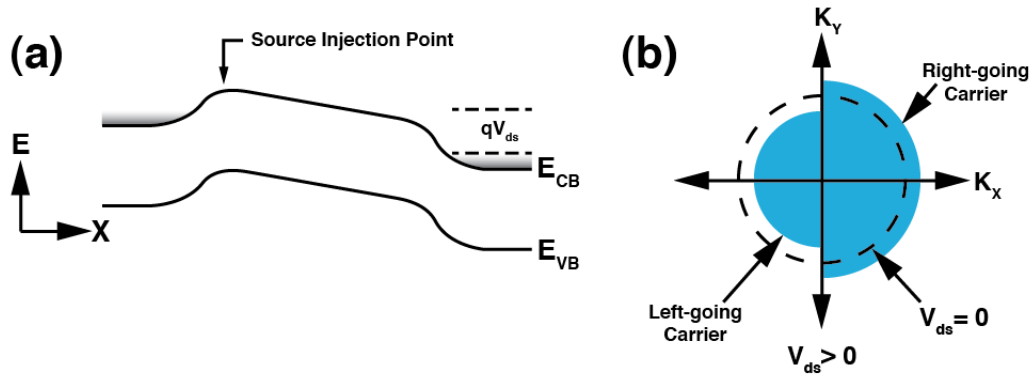


Figure 2.6: a) General band diagram of a FET in the source-drain direction with applied bias V_{ds} . b) Sketch of Fermi circle when bias is applied.

The current can be found at any point along the x axis in figure 2.6, but the source injection point is commonly chosen. The source injection point is indicated on the band diagram in figure 2.6 and one can see that at this point there is no electric field, which simplifies the calculations. The left-going and

right-going currents can be calculated by the following equations

$$J_{\rightarrow} = \frac{g_s g_v}{L^2} \sum_{k_x, k_y} v_{g\rightarrow}(k_x, k_y) f_{\rightarrow}(k_x, k_y) = \frac{g_s g_v}{(2\pi)^2} \int k dk d\theta v_{g\rightarrow}(k, \theta) f_{\rightarrow}(k), \quad (2.13)$$

$$J_{\leftarrow} = \frac{g_s g_v}{(2\pi)^2} \int k dk d\theta v_{g\leftarrow}(k, \theta) f_{\leftarrow}(k), \quad (2.14)$$

$$J_{Total} = J_{\rightarrow} - J_{\leftarrow}, \quad (2.15)$$

which is merely a summation of the current at each eigenstate converted into an integral. In the above equations, v_g is the electron group velocity (section 2.3), and $f = 1/(e^{\beta(E-E_f)} + 1)$ is electron occupation function. In the occupation function, terms can be consolidated by defining $\eta \equiv E_f/k_B T$ and there will be η_{\rightarrow} and η_{\leftarrow} for right and left-going carriers. The η_{\rightarrow} and η_{\leftarrow} are dependent upon the carrier densities of the right and left-going carriers. Therefore, to find these values at a particular bias, carrier conservation must be considered. The carrier densities under zero and non-zero drain bias can be found by summing over all occupied eigenstates. Converting to integral form, the equations are

$$n_s = \frac{g_s g_v}{L^2} \sum_{k_x, k_y} f(k_x, k_y) = \int_{E_c}^{\infty} dE g(E) f(E), \quad (2.16)$$

$$n_{\rightarrow} = \int_{E_c}^{\infty} dE g(E) f_{\rightarrow}(E), \quad (2.17)$$

$$n_{\leftarrow} = \int_{E_c}^{\infty} dE g(E) f_{\leftarrow}(E), \quad (2.18)$$

$$n_s = n_{\rightarrow} + n_{\leftarrow}. \quad (2.19)$$

Plugging equations 2.16, 2.17, and 2.18 into 2.19, one can solve $\eta_{\rightarrow}(V_{ds})$, where V_{ds} is the drain voltage relative to the grounded source. Subsequently, $\eta_{\leftarrow}(V_{ds})$ will also be found, because $\eta_{\leftarrow} = \eta_{\rightarrow} - qV_{ds}$. Now, η_{\rightarrow} and η_{\leftarrow} can be plugged into the current equations above to find the total current under any source-drain bias.

Up to this point, the carrier density of the semiconductor material has just been the materials intrinsic carrier density. However, in order to properly model a 2D FET device, one must account for the application of non-zero voltages to the top and bottom gates (figure 2.5). The addition of the top and bottom gate voltages allows control over the carrier density (equation 2.16) by injecting carriers into the channel via the source. This can be thought of as changing the area of the fermi circle in figures 2.5c and 2.6b.

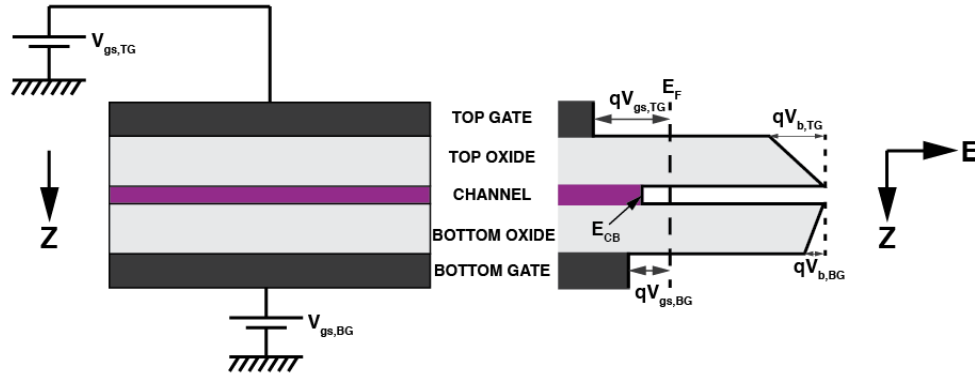


Figure 2.7: General band diagram of a double gate 2D FET in the direction of the gate-insulator-channel (chosen to be z-axis)

By summing over energies in the band diagram along the z axis (figure 2.7), the gate voltage dependent carrier density, $n_s(V_{gs})$, can be found. The current due to a source-drain voltage can be found using equations 2.13-2.19 in the same manner as before, with the only difference being the use of $n_s(V_{gs})$ instead of equation 2.16.

The specific application of this process to a silicene IDGFET is shown in the next chapter and a good demonstration of applying this model to 3D semiconductor FETs with parabolic band structures is given in [26]. It should be noted that this model assumes perfect gate control over the carrier density at the source injection point and neglects drain-induced barrier lowering.

CHAPTER 3

SILICENE ELECTRONIC PROPERTIES

With the necessary theoretical background reviewed, the electronic properties of silicene can now be understood. In this chapter, the electronic and topological properties of silicene that effect transport in devices are modeled and analyzed. How these properties change in the presence of a perpendicular electric field is discussed as well.

3.1 Band Structure of Silicene

As mentioned in section 2.1, a tight-binding model is a good method for analytically examining the band structure of a material. Due to the sublattices of silicene being separated from each other, application of an electric field perpendicular to the silicene sheet will create a potential difference between the two sublattices. Using a four-band model with second nearest neighbor coupling, a tight binding Hamiltonian can be derived. In second quantization formalism, this Hamiltonian is found to be [9, 28]

$$\begin{aligned}
 H = -t \sum_{\langle i,j \rangle \alpha} c_{i\alpha}^\dagger c_{j\alpha} + i \frac{\lambda_{SO}}{3\sqrt{3}} \sum_{\langle\langle i,j \rangle\rangle \alpha\beta} v_{ij} c_{i\alpha}^\dagger \sigma_{\alpha\beta}^z c_{j\beta} - i \frac{2}{3} \lambda_R \sum_{\langle\langle i,j \rangle\rangle \alpha\beta} \mu_{ij} c_{i\alpha}^\dagger (\vec{\sigma} \times \vec{d}_{ij}^0)_\alpha^\beta c_{j\beta} + \\
 e\ell \sum_{i\alpha} \zeta_i E_z^i c_{i\alpha}^\dagger c_{j\alpha},
 \end{aligned} \tag{3.1}$$

where the first term is the normal nearest neighbor hopping term with $t = 1.6$ eV being the hopping energy and $c_{i\alpha}^\dagger$ and $c_{i\alpha}$ being the electron creation and annihilation operators at site i with spin polarization α . The $\langle i, j \rangle$ term represents summing over nearest neighbors. The action of the first term is to cause electron hopping from between nearest neighbor sites, as shown in figure 3.1.

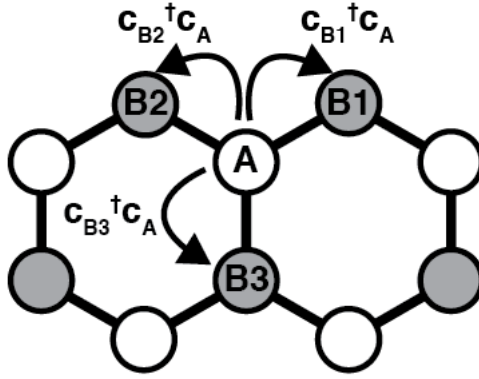


Figure 3.1: Action of the nearest neighbor creation/annihilation operators on the silicene lattice.

As denoted by the $\langle\langle i, j \rangle\rangle$ term, the second term represents second nearest neighbor spin orbit coupling where $\lambda_{so} = 3.9$ meV is the effective SOC constant, σ_i is the Pauli spin matrix, and $v_{ij} = (\vec{d}_i \times \vec{d}_j)/|\vec{d}_i \times \vec{d}_j|$ where \vec{d}_i and \vec{d}_j are the two bonds connecting the next nearest neighbors. The third term represents second nearest neighbor intrinsic Rashba spin orbit coupling where $\lambda_R = 0.7$ meV is the Rashba SOC constant, $\mu_{ij} = \pm 1$ represents the sublattice, and $\vec{d}_{ij}^0 = \vec{d}_{ij}/|\vec{d}_{ij}|$. The last term is the Hamiltonian modification due to the potential difference between the sublattices where $\zeta_i = \pm 1$ represents the sublattice, E_z is the strength of the electric field applied perpendicularly to the silicene plane, and $\ell = 0.23\text{\AA}$ is half the vertical distance between the sublattices. For a detailed derivation of this Hamiltonian, the reader is referred to [28].

For many solid state devices, the applied potentials are relatively low (~ 1 V or less) and thus result in low energy excitations in the band structure. Therefore, a low energy approximation to the Hamiltonian can be used to examine the physics in this regime. This gives the advantage of being much less computationally intensive and even analytical in many cases. For silicene, using

equation 3.1, a low energy effective Hamiltonian has been found to be [28]

$$H_\eta = \hbar v_f (k_x \tau_x - \eta k_y \tau_y) + \eta \tau_z h_{11} + e \ell E_z \tau_z, \quad (3.2)$$

where $v_f = \frac{\sqrt{3}at}{2\hbar} = 5.5 \times 10^7$ cm/s is the Fermi velocity, $a = 3.86$ Å is the lattice constant, τ_i is the Pauli sublattice matrix, $\eta = \pm 1$ refers to the K_\pm Dirac point, and h_{11} is

$$h_{11} = -\lambda_{SO} \sigma_z - a \lambda_R (k_y \sigma_x - k_x \sigma_y). \quad (3.3)$$

As mentioned by Liu [28], the effective Hamiltonian can be found by Fourier transforming the creation and annihilation operators in equation 3.1 and summing over nearest and next-nearest neighbors. This converts the Hamiltonian to a momentum space representation, which is then expanded about the Dirac points to achieve the low energy approximation given in equation 3.2. This expansion pulls the extra terms found in equation 3.2 (k_x, k_y, v_f) out of the phase factors in the Hamiltonian. The effective Hamiltonian can also be derived using tight-binding with an atomic orbital bases, which is also shown in [28].

At each Dirac point, the matrix created from equations 3.2 and 3.3 can be diagonalized to find the energy dispersion at energies near that of the Dirac points. This energy dispersion can be compactly written as [9]

$$E_\eta = \pm \sqrt{\hbar^2 v_f^2 k^2 + \left(e \ell E_z - \eta s_z \sqrt{\lambda_{SO}^2 + a^2 \lambda_R^2} k^2 \right)^2}, \quad (3.4)$$

where $s_z = \pm 1$ refers to spin up and spin down states. Equation 3.4 takes on a form similar to that of graphene (equation 2.2), but with an additional mass term shown in the parenthesis. Furthermore, this mass can be adjusted by tuning the value of E_z and its effect on the band structure will be different for spin up and spin down states, meaning that the energy dispersion will differ for spin up and spin down states. This creates a gap $E_{gap}^\sigma = E_\uparrow - E_\downarrow$ between spin up and spin down bands.

The energy dispersion near the K_+ and K_- Dirac points are plotted in figure 3.2 at various values of E_z . One can see that at $E_z = 0$ the bands are spin and valley degenerate and there is a band gap of ~ 7.8 meV. When $|E_z|$ is increased, spin degeneracy is broken and the bands split into distinct spin up and spin down states. This is expected since the application of a perpendicular electric field creates a potential difference between the two sublattices.

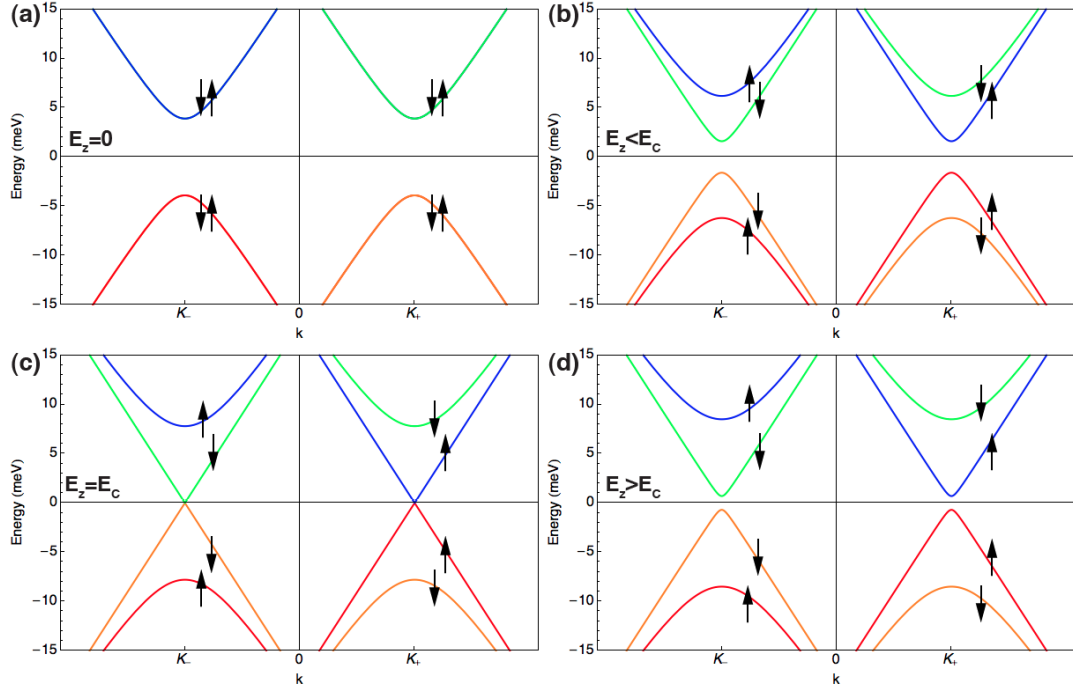


Figure 3.2: Silicene low-energy band structure at a) $E_z = 0$, b) $E_z < E_c$, and c) $E_z = E_c$, and d) $E_z > E_c$. Arrows indicate spin.

Near the K_+ Dirac point, as E_z increases from zero the band gap of the spin up states decrease while the gap of the spin down states increase. This continues until E_z reaches the critical value $E_c = \lambda_{SO}/e\ell \approx 17$ mV/ \AA , at which the spin up energy dispersion becomes completely gapless and similar to that of graphene. Beyond this point, the gap in the spin up dispersion re-opens and continues to increase as E_z increases. When E_z is decreased below zero, the spin up band that becomes gapless at $-E_c$. Near the K_- Dirac point, the modified spin states are

opposite that of the K_+ Dirac point.

Observing figure 3.2, it can be seen that there are two notable regimes that can be considered: $|E_z| < |E_c|$ and $|E_z| > |E_c|$. The transition from one regime to the other occurs as E_z sweeps through E_c and the band gap closes and re-opens. As mentioned in section 2.4, the closing and opening of a band gap signifies a non-smooth change in the material's Hamiltonian and a topological phase change in its eigenvalue spectrum. In the subsequent sections, this topological phase change will be confirmed by finding the Z_2 invariant in these two regimes.

Considering that the Rashba component has a negligibly small effect on the properties of silicene being investigated in this thesis, from this point forward the Rashba spin orbit component will be neglected. In the parenthesis of equation 3.4, the λ_{SO}^2 term is on the order of 10 meV^2 while the $a^2 \lambda_R^2 k^2$ term is on the order of 10^{-4} meV^2 at $k = 0.5 \text{ nm}^{-1}$. As we will see in section 3.3, the unique properties generally occur close to the Dirac points ($< 0.5 \text{ nm}^{-1}$). Therefore, if one sets $\lambda_R = 0 \text{ meV}$ in equation 3.4, the band structure remains relatively unchanged.

3.2 Density of States

In consideration of the prominent role that carrier density plays in determining the transport properties of devices, examining the low energy density of states (DOS) in silicene will be beneficial in the next chapter. Generally, the density of states can be found by equating the number of states in a infinitesimal volume

of k space to that of energy space

$$\frac{2\pi g_s g_v}{(\frac{2\pi}{L})^2} k dk = G(E) dE, \quad (3.5)$$

where $G(E)$ is the total density of states and g_s and g_v are the spin and valley degeneracy. Since the degeneracy of silicene changes depending on the applied electric field, the DOS must be found for each band separately and summed to achieve the total DOS. Therefore, for each separate band $g_s = g_v = 1$.

Using equation 3.4, the left side of equation 3.5 can be converted to energy space and used to solve for the DOS per unit area, $g(E) = G(E)/L^2$. For the spin up states near the K_+ Dirac point, this yields the following

$$\frac{1}{2\pi} k \frac{\sqrt{\hbar^2 k^2 v_f^2 + (eE_z \ell - \lambda_{so})^2}}{\hbar^2 k v_f^2} dE = g(E) dE \rightarrow g_{+\uparrow}(E) = \frac{|E|}{2\pi \hbar^2 v_f^2} \Theta(|E| - |eE_z \ell - \lambda_{so}|), \quad (3.6)$$

where $g_{+\uparrow}(E)$ signifies the DOS of spin up states near the K_+ Dirac point. The step function is required to account for the fact that states can not exist in the band gap of the material and the absolute value signs in the step function account for the valance and conduction bands. Similarly, for spin down states near the K_+ Dirac point

$$g_{+\downarrow}(E) = \frac{|E|}{2\pi \hbar^2 v_f^2} \Theta(|E| - |eE_z \ell + \lambda_{so}|). \quad (3.7)$$

Due to the symmetry of the bands, which can be seen in figure 3.2, the density of states near the K_- Dirac point will have the following relations

$$g_{-\uparrow} = g_{+\downarrow}, \quad (3.8)$$

$$g_{-\downarrow} = g_{+\uparrow}, \quad (3.9)$$

and the total DOS will be the sum of the DOS over all bands

$$g_{total}(E) = \sum_{\eta, s_z} g_{\eta, s_z}(E) = \frac{|E|}{\pi \hbar^2 v_f^2} \left(\Theta(|E| - |eE_z \ell + \lambda_{so}|) + \Theta(|E| - |eE_z \ell - \lambda_{so}|) \right). \quad (3.10)$$

The total DOS at various electric field strengths can be seen in figure 3.3. At $E_z = 0$, the bands are spin degenerate, resulting in only one step and then a linear DOS. When $E_z \neq 0$ two steps occur in the DOS since the bands are split into upper and lower bands. As $|E_z|$ approaches $|E_c|$, the first step decreases until it is zero at $|E_z| = |E_c|$. At this point, the DOS of the first bands match that of graphene since the lower bands themselves are of the same form as graphene. As $|E_z|$ increases beyond $|E_c|$, the first step in the DOS re-opens and continues to grow larger as $|E_z|$ increases. This behavior precisely matches that of the band structure. One can also see from figure 3.3 that the DOS is always linear. The reason for this is unclear, but this is a surprising result, as one would expect the DOS near the band edge to be constant due to the parabolic nature of the bands near the edge. In the next chapter, the effects that this DOS manipulation has on current in a FET device will be explored.

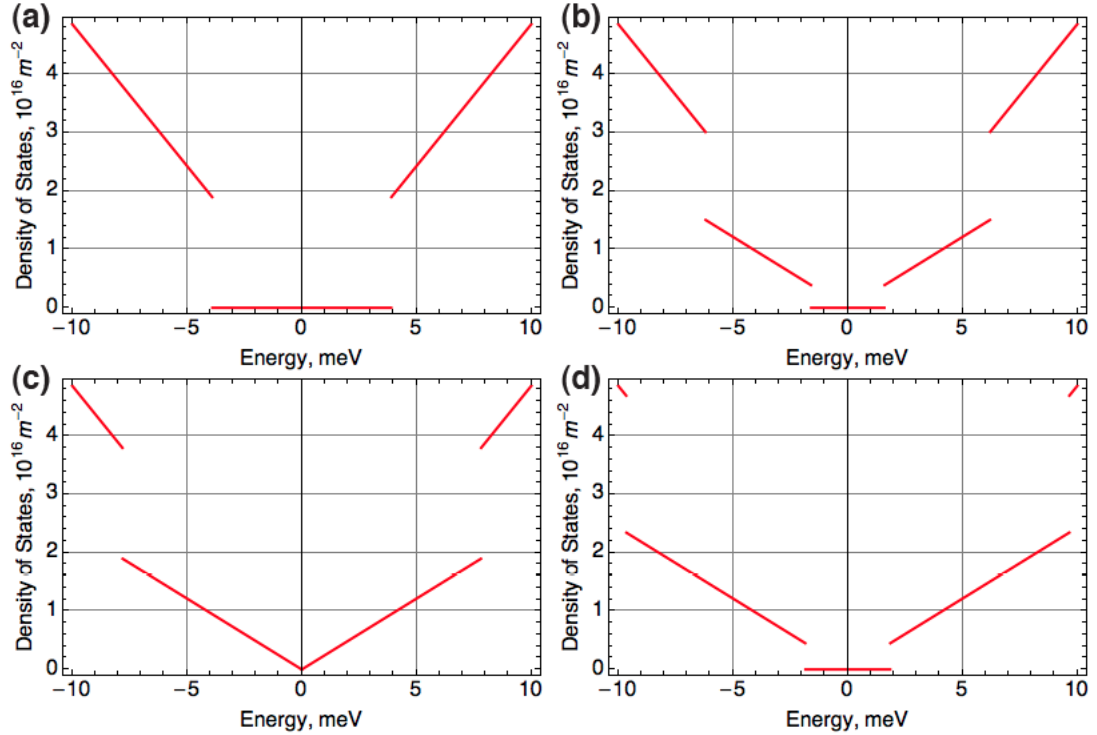


Figure 3.3: Total DOS at a) $E_z = 0$, b) $|E_z| < |E_c|$, c) $|E_z| = |E_c|$, and d) $|E_z| > |E_c|$

3.3 Berry Curvature

As discussed in the previous chapter, a non-trivial Berry curvature can greatly influence the transport and topological properties of a material. Therefore, investigating the Berry curvature of silicene is a natural precursor to understanding silicene in a device setting. Using equation 2.8, one can calculate the berry curvature for any material. It can also be found using equation 2.7, but equation 2.8 doesn't require differentiation of the eigenstates and is therefore easier for computational software to handle.

The eigenstates of silicene are found by computationally solving for the eigenvectors of the Hamiltonian given in equation 3.2. Upon normalization, the Hamiltonian must be differentiated according to equation 2.8. For three dimensional k-space, the differentiation gives

$$\frac{\partial H}{\partial k_x} = \hbar v_f \tau_x + \eta a \lambda_R \sigma_y, \quad (3.11)$$

$$\frac{\partial H}{\partial k_y} = -\eta \hbar v_f \tau_y - \eta a \lambda_R \sigma_x, \quad (3.12)$$

$$\frac{\partial H}{\partial k_z} = 0, \quad (3.13)$$

which means that the only non-zero Berry curvature will be Ω_{xy}^n . Therefore, the Berry curvature for silicene will always be in the z direction.

Plugging equations 3.11 and 3.12 into equation 2.8, the Berry curvature is found for each band by summing over the interactions between the band of interest and all other bands. With the Rashba SO component neglected, it is found that there are only interactions between the valence and conduction bands. With the Rashba SO component included, there are interactions between two valence or conduction bands, but they are negligible compared to the interactions when

one band is conduction and the other is valence. It is found that the Berry curvature of silicene can be expressed in the following compact form

$$\Omega_{xy} = \frac{\xi \eta \hbar^2 v_f^2 (e E_z \ell - \eta s_z \lambda_{SO})}{2(\hbar^2 k^2 v_f^2 + (-\eta s_z e E_z \ell + \lambda_{SO})^2)^{3/2}} \hat{z}, \quad (3.14)$$

where $k = \sqrt{k_x^2 + k_y^2}$ and $\xi = \pm 1$ signifies the conduction and valence bands. Also, $\eta = \pm 1$ and $s_z = \pm 1$ again signify the Dirac points and spin states.

The conduction band Berry curvature near the K_+ Dirac point can be seen in figure 3.3. At $E_z = 0$, the Berry curvature for the spin up and spin down states are equal magnitude, but opposite direction. Also, the maximum curvature is always reached at the Dirac point. As seen in figure 3.4, increasing the field strength causes the curvature of one spin state to increase while the other spin state decreases. Which spin state increases depends on the direction of the field. Figure 3.3 shows the results of increasing the field strength in the positive z direction.

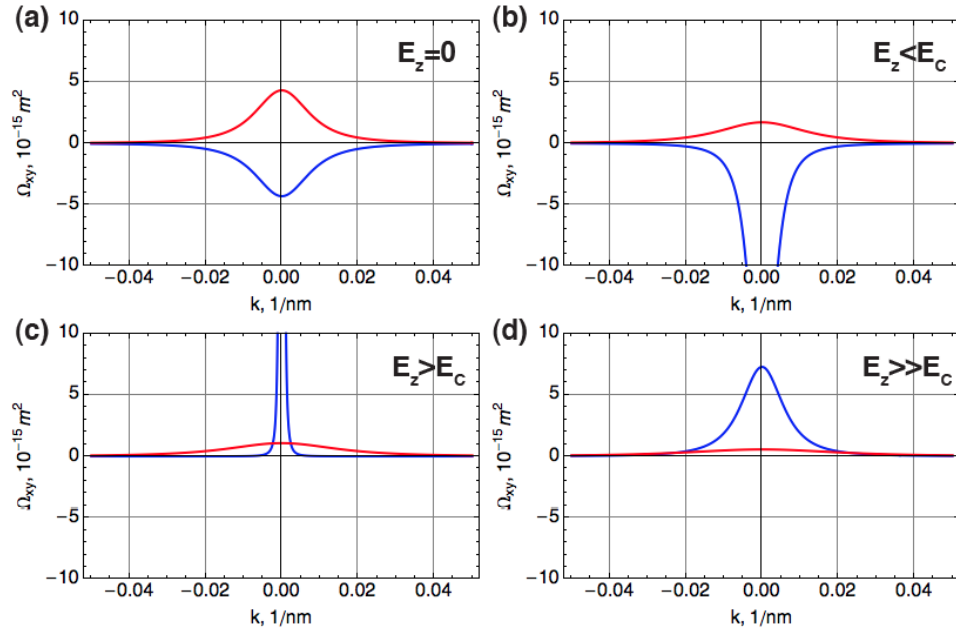


Figure 3.4: Spin up (blue) and spin down (red) conduction band Berry curvature near K_+ at a) $E_z = 0$, b) $E_z < E_c$, c) $E_z > E_c$, and d) $E_z \gg E_c$

As E_z approaches E_c , the spin up Berry curvature in figure 3.4 diverges while the spin down curvature continues to decrease. When E_z become greater than E_c , the direction of the spin up Berry curvature changes sign and decreases in magnitude as E_z is increased beyond this point. Therefore, E_c is the critical point at which the spin up and spin down Berry curvatures transition from pointing in opposite direction to pointing in the same direction. If the electric field strength is increased in the negative z direction the same phenomena occurs. However, under this field it is the spin down curvature that diverges and changes direction as E_z is swept through E_c .

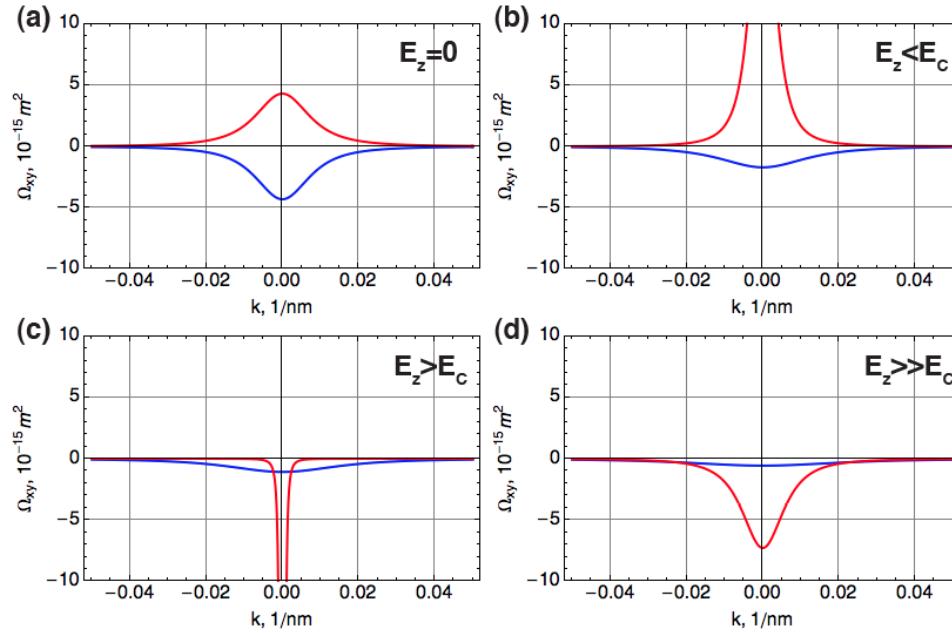


Figure 3.5: Spin up (blue) and spin down (red) conduction band Berry curvature near K_- at a) $E_z = 0$, b) $E_z < E_c$, c) $E_z > E_c$, and d) $E_z \gg E_c$

As seen in figure 3.5, the Berry curvature near the K_- Dirac point when E_z is increased in the positive z direction following the same pattern. However, the spin state which switches direction when E_z is swept through E_c is opposite that near the K_+ Dirac point. In subsequent sections it will be shown that this difference creates very interesting transport properties in silicene.

3.4 Z_2 Topological Invariant

In order to gain better insight into the properties of a unique material like silicene, it is very useful to characterize the material's topological phase. It has been claimed that silicene is a topological insulator when $|E_z| < |E_c|$ and that it transitions to a band insulator when $|E_z| > |E_c|$ [9]. However, there is little in the way of theoretical calculations to support this. Therefore, with Berry curvature of silicene found it is a prudent time to examine silicene's topological phase by calculating the Z_2 invariant.

As described in section 2.4, since s_z is conserved in this low energy approximation of silicene's band structure, the use of spin Chern numbers is a convenient method to find the Z_2 invariant. Using equation 2.10, $n_m = \frac{1}{2\pi} \int_{FBZ} d^2\mathbf{k} \Omega_m(\mathbf{k})$, and plugging the Berry curvatures of each occupied (valence) band (equation 3.14), the Z_2 invariant can be found. The partial Chern number for spin up valence band near K_+ is found to be

$$n_{+, \uparrow} = \frac{1}{2\pi} \int_0^\infty dk \frac{-\hbar^2 v_f^2 (eE_z \ell - \lambda_{SO})}{2(\hbar^2 k^2 v_f^2 + (-eE_z \ell + \lambda_{SO})^2)^{3/2}} = \frac{-eE_z \ell + \lambda_{SO}}{2\sqrt{(-eE_z \ell + \lambda_{SO})^2}}. \quad (3.15)$$

Equation 3.15 is referred to as a "partial Chern number", because only the K_+ valley is considered. The Chern number of this band is found by summing the partial Chern number over the two valleys. It must be noted that the partial Chern numbers are not physically meaningful; they are merely being used as an intermediary step to better elucidate the process. Using the same method, partial Chern number expressions can be found for the rest of the bands as well and can be placed in the following compact form

$$n_{\xi, \eta, s_z} = \frac{\xi(\eta e E_z \ell - s_z \lambda_{SO})}{2\sqrt{(-\eta s_z e E_z \ell + \lambda_{SO})^2}}, \quad (3.16)$$

where $\xi = \pm 1$ represents the conduction and valance bands, $\eta = \pm 1$ represents the Dirac points, E_z is the vertical electric field, $\lambda_{SO} = 3.9$ meV is the effective SOC constant, and $\ell = 0.23$ Å is half the distance between the sublattices.

From equation 3.16, since each band's Chern number is the sum over the two valleys, each band's Chern number will always be ± 1 . This is shown in figure 3.6, in which the magnitude of the partial Chern number is always $\pm 1/2$ for every band near a single valley. For each band, there is also a critical electric field strength at which the Chern number changes sign. This critical field occurs at $E_z = \lambda_{SO}/e\ell$, which is the electric field at which the band gap for one spin state is reduced to zero.

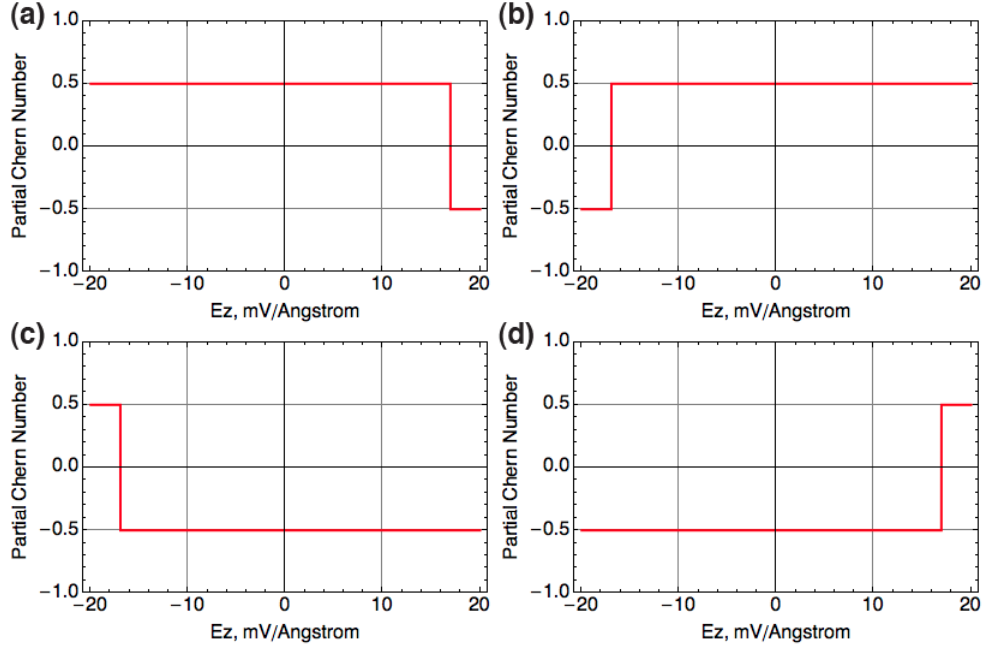


Figure 3.6: Partial Chern numbers for a) spin up states near K_+ , b) spin up states near K_- , c) spin down states near K_+ , and d) spin down states near K_-

Using the results of figure 3.6 along with equations 2.11, $\nu = n_\sigma \bmod 2$, the Z_2 invariant can be calculated. It should also be noted that the Chern invariant, which is merely the sum of the Chern numbers, is always zero. Therefore, before

calculating the Z_2 invariant it is already clear that the electronic phase of silicene must either be a band insulator or a topological insulator. A plot of the spin chern number difference, $n_\sigma = (n_\uparrow - n_\downarrow)/2$, is shown in figure 3.7. Using equation 2.11, it can be seen that when $|E_z| < |E_c|$ the Z_2 invariant is that of a topological insulator. When $|E_z| > |E_c|$, the Z_2 invariant changes to that of a band insulator. Therefore, it has been confirmed that silicene does indeed transition from topological insulator to band insulator when E_z is swept through E_c . It should be noted that although this model characterizes silicene in these two topological regimes, the topological properties of silicene when $E_z = E_c = \lambda_{SO}/e\ell$ are not clearly characterized by this model.

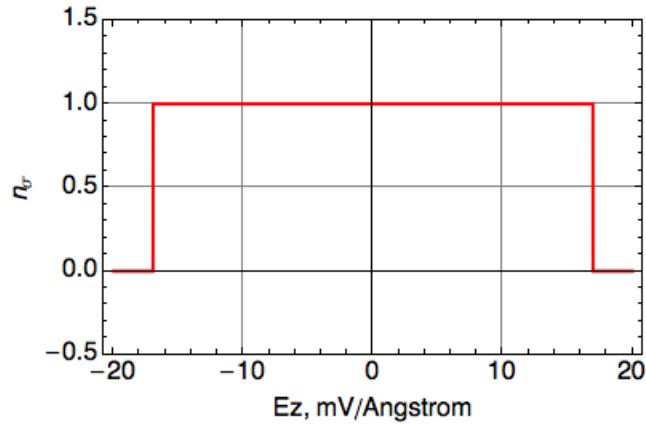


Figure 3.7: Spin chern number difference, n_σ , versus perpendicular electric field

3.5 Electron Velocity

In order to examine ballistic transport in a silicene FET, the group velocity of the electron states in silicene must first be known. As discussed in section 2.3, most common materials have a electron velocity that is found by simply taking the gradient of the energy dispersion. However, when a material has a non-trivial

Berry curvature, an extra term is required to properly characterize the velocity profile. As seen in equation 2.9, $\mathbf{v}_n(\mathbf{k}) = \frac{\partial \varepsilon_n(\mathbf{k})}{\hbar \partial \mathbf{k}} - \frac{e}{\hbar} \mathbf{E} \times \boldsymbol{\Omega}_n(\mathbf{k})$, this term depends on a cross product of the applied electric field as well as the Berry curvature. Since the Berry curvature in silicene is solely in the z direction, the z direction electric field that has been used to modify the properties of silicene thus far will not contribute directly to the electron velocity since $E_z \hat{z} \times \boldsymbol{\Omega}_{xy} \hat{z} = 0$. Therefore, it will be assumed henceforth that an electric field in the x direction is also being applied, which is the case for transport of carriers in the silicene plane. For now, this field will have an arbitrary magnitude, but in the next chapter E_x and E_z will be dictated by the voltages applied to the drain and gate contacts. Using the band structure and Berry curvature of silicene in equation 2.9, the electron group velocity components in the conduction band are found to be

$$v_{x,\eta,s_z} = \frac{\partial \varepsilon_{\eta,s_z}(\mathbf{k})}{\hbar \partial k_x} = \frac{\hbar k_x v_f^2}{\sqrt{\hbar^2 k^2 v_f^2 + (-\eta s_z e E_z \ell + \lambda_{SO})^2}} \hat{x}, \quad (3.17)$$

$$v_{yOriginal} = \frac{\partial \varepsilon_{\eta,s_z}(\mathbf{k})}{\hbar \partial k_y} = \frac{\hbar k_y v_f^2}{\sqrt{\hbar^2 k^2 v_f^2 + (-\eta s_z e E_z \ell + \lambda_{SO})^2}} \hat{y}, \quad (3.18)$$

$$v_{yBerry,\eta,s_z} = -\frac{e}{\hbar} E_x \hat{x} \times \boldsymbol{\Omega}_{\eta,s_z}(\mathbf{k}) \hat{z} = -\frac{\eta e E_x \hbar v_f^2 (e E_z \ell - \eta s_z \lambda_{SO})}{2(\hbar^2 k^2 v_f^2 + (-\eta s_z e E_z \ell + \lambda_{SO})^2)^{3/2}} \hat{y}, \quad (3.19)$$

where $v_y = v_{yOriginal} + v_{yBerry}$. The Berry curvature velocity component, v_{yBerry,η,s_z} , can also be recast as

$$v_{yBerry,\eta,s_z} = -\mu_{B,\eta,s_z} E_x, \quad (3.20)$$

where μ_B is

$$\mu_{B,\eta,s_z} = -\frac{\eta e \hbar v_f^2 (e E_z \ell - \eta s_z \lambda_{SO})}{2(\hbar^2 k^2 v_f^2 + (-\eta s_z e E_z \ell + \lambda_{SO})^2)^{3/2}}. \quad (3.21)$$

In this form, μ_B can be considered to be an effective transverse mobility, or "Berry" mobility.

Since the current generating electric field is chosen to be in the negative x direction, which will be the case in the FET structure in the following chapter, the velocity component due to the Berry curvature will solely be in the y direction. Without the Berry curvature component, the velocity would be directed radially outward from the Dirac point in a similar manner to that of graphene. However, the Berry curvature velocity component greatly increases v_y near the Dirac points. As seen in figure 3.8, this creates a asymmetry in the velocity dispersion. Refer to appendix A for the velocity profiles of the remaining bands.

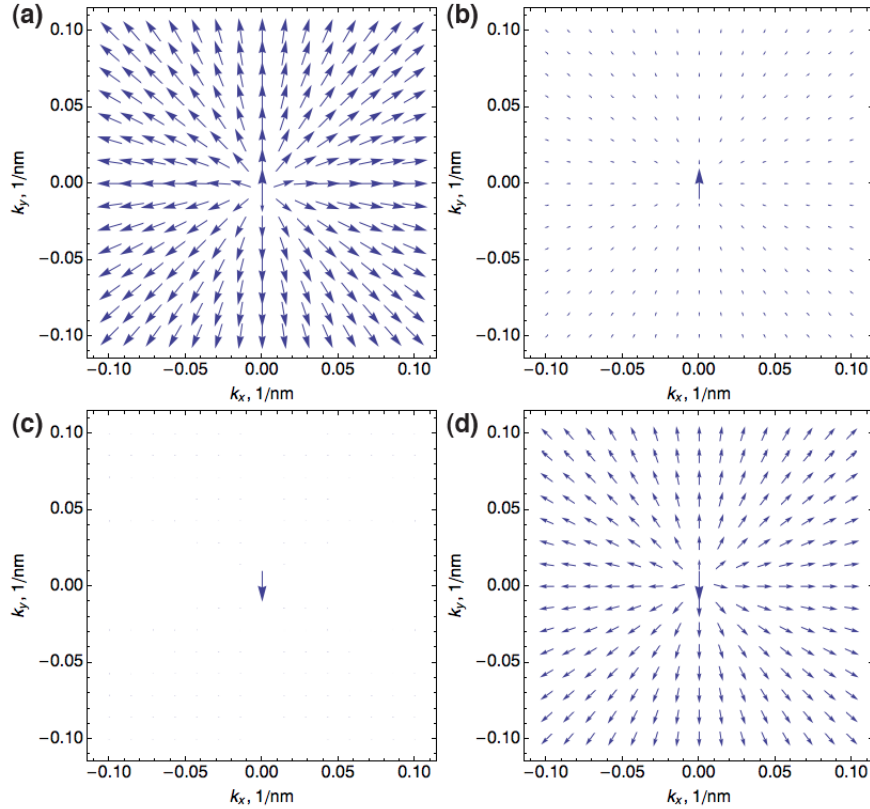


Figure 3.8: Spin up conduction band velocity profile near K_+ Dirac point at a) $E_z = 0$, b) $E_z < E_c$, $E_z > E_c$, and d) $E_z \gg E_c$. The length of the arrows are proportional to the magnitude of the velocities.

When $E_x \neq 0$ and $|E_z| \neq \lambda_{SO}/e\ell$, there is always an extra non-zero y component in the velocity due to the Berry curvature. This creates the previously

mentioned asymmetry in the velocity profile and also shifts the zero-velocity point away from the Dirac points. The Berry curvature velocity term quickly goes to zero as one moves away from the Dirac points and therefore reinforces the prediction that much of the interesting properties of silicene occur in the low-energy regime. Furthermore, when $|E_z| < |E_c|$ the y direction velocity of spin up and spin down states point in opposite directions and when $|E_z| > |E_c|$ the y direction velocities transition to pointing in the same direction.

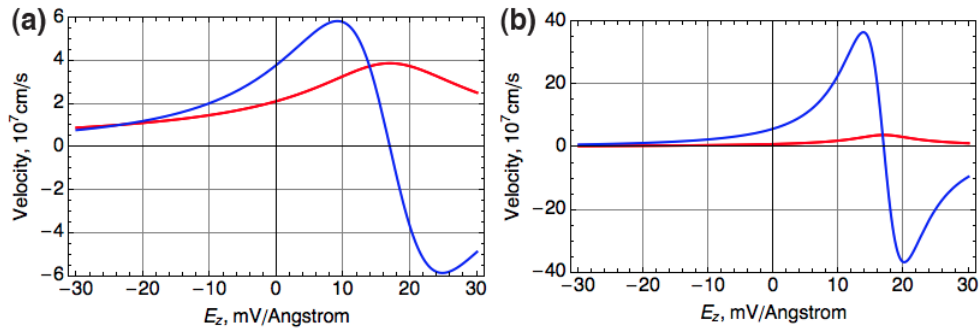


Figure 3.9: Spin up conduction band velocity profile of standard (red) and Berry (blue) velocities near K_+ Dirac point at a) $k_x = k_y = 5 \times 10^{-3} \text{ nm}^{-1}$, and b) $k_x = k_y = 2 \times 10^{-3} \text{ nm}^{-1}$.

As seen in figure 3.9a, initially the Berry velocity and standard group velocity are in the same direction. However, as E_z is increased the Berry velocity crosses the standard group velocity and eventually becomes negative and larger in magnitude than the standard velocity. This causes the transitioning in the y direction velocity near the Dirac points. Also, from figure 3.9b one can see that the transition becomes more abrupt as one gets closer to the Dirac point. At $k_x = k_y = 2 \times 10^{-3} \text{ nm}^{-1}$, the process resembles a switching effect more so than a smooth transition.

As will be examined in the next chapter, this transitioning in the velocity profile predicts a transitioning in the direction and magnitude of a spin Hall effect when silicene changes phase from topological insulator to band insulator.

Also, it should be noted that these Hall effects are being created without the use of a magnetic field, which is a unique property of topological insulators.

CHAPTER 4

SILICENE 2D FET MODELING & RESULTS

With the pertinent material properties of silicene explored in the previous section, these properties can now be used to examine silicene-based device physics. In this section, a model is developed to examine the transport properties of a silicene FET. The development of this model is based on the method originally created by Natori [26]. This method is modified to support the use of silicene as the channel material and the use of independent double gates.

4.1 Carrier Density

When examining the transport properties of any FET device, the goal is to find a relationship between the applied voltages (gate and drain voltages) and current density. As discussed in section 2.3, in order to find the current density, one must first find the relationship between the gate and drain voltages and the Fermi level at the source injection point. This relationship can be found by noting that application of a drain bias will not effect the total carrier density at the source injection point in a carefully designed transistor that has no short channel effects. Therefore, one can find the source injection point Fermi level by finding the relationship between the gate voltage and total carrier density and imposing carrier density conservation when a drain bias is applied.

Using the z direction band diagram (figure 2.7), one can find the relationship between gate voltages and carrier density by summing over energies. The carrier densities on the gates will be in the form of sheet charges and since we are dealing with a 2D material it can be assumed that the carrier density in the

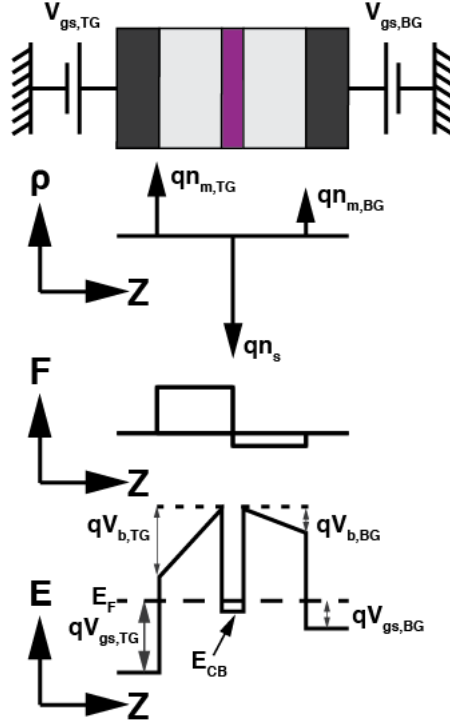


Figure 4.1: (a) charge, (b) field, and (c) band diagram of a general 2D independent double gate FET in the gate-channel-gate direction

channel will also be a sheet charge. This leads to the charge-field-barrier diagram shown in figure 4.1. By summing over the energies of the two barriers separately, one finds the following relations

$$q\phi_{b,TG} + qV_{b,TG} - \Delta E_C + (E_f - E_C) = V_{gs,TG}, \quad (4.1)$$

$$q\phi_{b,BG} + qV_{b,BG} - \Delta E_C + (E_f - E_C) = V_{gs,BG}, \quad (4.2)$$

where $q\phi_b$ is the metal-insulator barrier height, V_b is the voltage drop across the insulator (as seen in figure 2.7), ΔE_C is the insulator-semiconductor conduction band difference, E_f is the semiconductor Fermi level, and E_C is the intrinsic conduction band edge. Using Gauss' law, V_b is found to be equal to $qn_m/\epsilon_b\epsilon_0$. Grouping ϕ_b and ΔE_C into a threshold voltage term, $qV_T = q\phi_b - \Delta E_C$, equations

4.1 and 4.2 can be re-written as

$$\frac{q^2(n_s - n_{m,BG})}{\varepsilon_{b,TG}\varepsilon_0} + (E_f - E_C) = q(V_{gs,TG} - V_{T,TG}), \quad (4.3)$$

$$\frac{q^2 n_{m,BG}}{\varepsilon_{b,BG}\varepsilon_0} + (E_f - E_C) = q(V_{gs,BG} - V_{T,BG}), \quad (4.4)$$

where the charge neutrality condition, $n_s = n_{m,TG} + n_{m,BG}$, has been used in the first term of equation 4.3. From this point forward, the threshold voltage terms will not be written, but it will always be assumed that the gate voltages are in reference to the threshold voltages.

Re-arranging equation 4.4 and plugging it into $n_{m,BG}$ of equation 4.3, the relation between the gate voltages and total carrier density is found to be

$$\frac{qn_s}{\varepsilon_{b,TG}\varepsilon_0} + (1 + G)(E_f - E_{CB}) = V_{gs,TG} + GV_{gs,BG}, \quad (4.5)$$

$$G = \frac{\varepsilon_{b,BG}t_{b,TG}}{t_{b,BG}\varepsilon_{b,TG}}, \quad (4.6)$$

in which n_s is the total carrier density in the semiconductor, $t_{b,TG}$ and $t_{b,BG}$ are the top and bottom gate oxide thickness, $\varepsilon_{b,TG}$ and $\varepsilon_{b,BG}$ are the top and bottom gate oxide relative permittivity, and $V_{gs,TG}$ and $V_{gs,BG}$ are the top and bottom gate voltages (referenced to the grounded source).

By applying equation 2.16, $n_s = \int_{E_c}^{\infty} dE g(E) f(E)$, to silicene, a relationship can be found between n_s and E_f . This relationship can be plugged into equation 4.5 to find $n_s(V_{gs,TG}, V_{gs,BG})$. Alternatively, this relationship could be also be used to find $E_F(V_{gs,TG}, V_{gs,BG})$, which is be found to be a less computationally intensive method for finding η_R and η_L when a drain bias is applied. Applying equation 2.16 to silicene, the following relation is found

$$n_{\eta,s_z} = \frac{1}{\pi v_f^2 \hbar^2} \int_{E_{CB}}^{\infty} dE \frac{E}{1 + e^{(E-E_f)/k_b T}} = \frac{k_b^2 T^2}{\pi v_f^2 \hbar^2} \int_{\beta E_{CB}}^{\infty} du \frac{u}{1 + e^{u-\eta_0}}, \quad (4.7)$$

$$n_s = \sum_{\eta} \sum_{s_z} n_{\eta, s_z} = 2(n_{+, \uparrow} + n_{+, \downarrow}), \quad (4.8)$$

where $E_{CB} = |eE_z \ell - \eta s_z \lambda_{SO}|$ is the conduction band edge and the $2(n_{+, \uparrow} + n_{+, \downarrow})$ in equation 4.8 results from the symmetry of the bands. The last term in equation 4.7 comes from changing to the dimensionless variable $u = E/k_b T$. These equations can not be solved analytically as they contain Fermi-Dirac integrals of order one. Therefore, equation 4.8 must be solved computationally to find $E_f(n_s)$. Plugging this into E_f in equation 4.5, one can computationally solve for $n_s(V_{gs, TG}, V_{gs, BG})$. In order to find E_z , the electric field is assumed to linearly change through the channel and the mid-point found to be

$$E_z = \frac{1}{2} \left(\frac{V_{gs, BG}}{t_{b, BG}} - \frac{V_{gs, TG}}{t_{b, TG}} \right), \quad (4.9)$$

which is taken as the vertical field to which the channel is exposed. Figure 4.2 shows the conduction band carrier density found for $t_{b, TG} = t_{b, BG} = 2$ nm and $\epsilon_{b, TG} = \epsilon_{b, BG} = 10$.

One can see from figure 4.2 that the carrier density depends on the gate voltages as would be expected in a FET device. Increasing the positive gate voltage on either gate injects more carriers into the channel via the source. As either of the gate voltages becomes much less than zero, the carriers are pulled out of the channel and the carrier density approaches zero. Furthermore, temperature only has a notable effect at lower gate voltages. At higher voltages the carrier density is high enough that temperature changes don't make notable changes to the carrier density, because $E_f - E_c \gg k_b T$.

As previously discussed, when a drain bias is applied the right-going and left going carriers will have different quasi-Fermi levels. The difference between these quasi-Fermi levels is equal to the drain bias in the ballistic approximation and they can be found by imposing carrier density conservation, $n_s = n_{\rightarrow} + n_{\leftarrow}$.

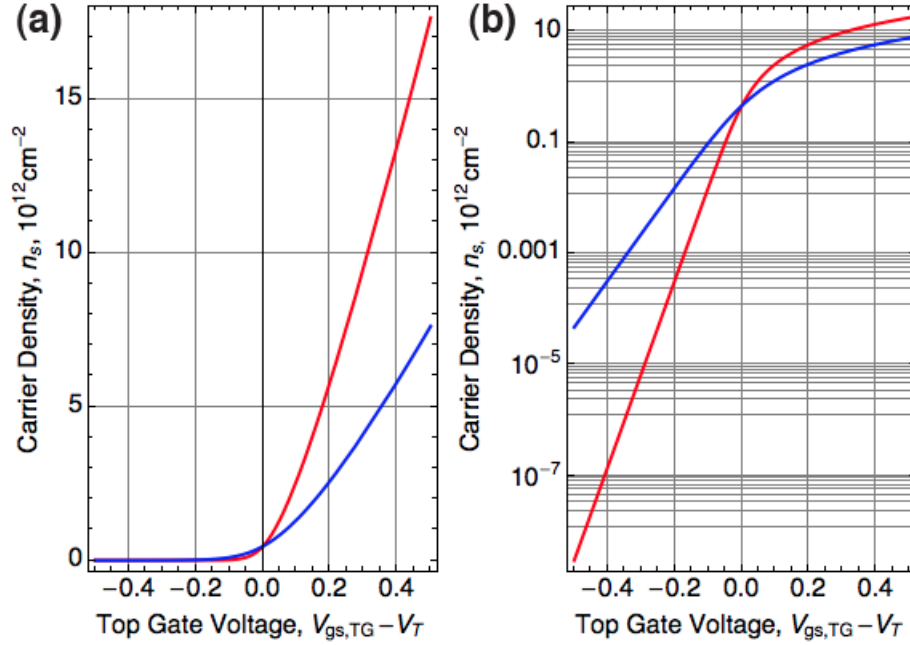


Figure 4.2: Carrier density at 300K and $V_{gs,TG} = V_{gs,BG}$ (red) and $V_{gs,BG} = 0$ (blue)

Since the application of an electric field causes the bands to break degeneracy, the carrier density conservation is imposed on a per-band basis. Therefore, when applying a drain bias the carrier density is split into right-going and left-going carrier densities as follows

$$n_{\eta,s_z} = \frac{k_b^2 T^2}{\pi v_f^2 \hbar^2} \int_{\beta E_{CB}}^{\infty} du \frac{u}{1 + e^{u-\eta_0}} = \frac{k_b^2 T^2}{2\pi v_f^2 \hbar^2} \int_{\beta E_{CB}}^{\infty} du \left(\frac{u}{1 + e^{u-\eta_{\rightarrow}}} + \frac{u}{1 + e^{u-\eta_{\leftarrow}}}} \right), \quad (4.10)$$

where the first term of equation 4.10 is just equation 4.7 and must equal the right hand side due to carrier density conservation. The carrier density without drain bias for each band can be found using the total carrier density, n_s , to find the Fermi level from $E_f(n_s)$ and plugging this into η_0 . Therefore, since $\eta_{\leftarrow} = \eta_{\rightarrow} - qV_{ds}$, the only unknown in equation 4.10 is η_{\rightarrow} .

Using equation 4.5 to find n_s , η_{\rightarrow} is computationally found and used to calculate current density in the next section. Figure 4.3 shows total carrier density as a function of drain bias. As expected, the total carrier density is only dependent

on the gate and has no dependence on drain bias.

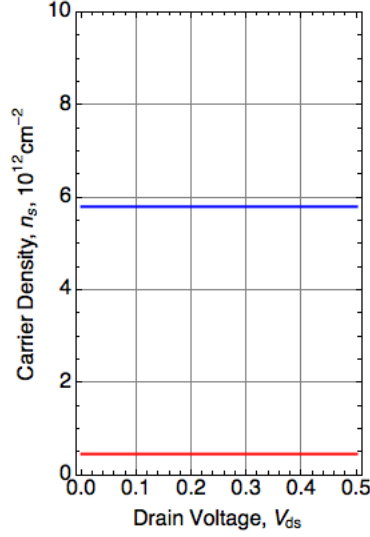


Figure 4.3: Carrier density at 300K and $V_{gs,TG} = V_{gs,BG} = 0$ V (red) and $V_{gs,TG} = V_{gs,BG} = 0.2$ V (blue)

4.2 Conventional Source-Drain Current

Using $\eta_{\rightarrow}(V_{ds}, V_{TG,gs}, V_{B,gs}) = E_f/k_B T$, the total drain charge current can be found using equations 2.13-2.15,

$$J_{\rightarrow} = \frac{eg_sg_v}{(2\pi)^2} \int kdkd\theta v_{g\rightarrow}(k, \theta) f_{\rightarrow}(k), \quad (2.13)$$

$$J_{\leftarrow} = \frac{eg_sg_v}{(2\pi)^2} \int kdkd\theta v_{g\leftarrow}(k, \theta) f_{\leftarrow}(k), \quad (2.14)$$

$$J_{Total} = J_{\rightarrow} - J_{\leftarrow}. \quad (2.15)$$

As before, the current is found on a per-band basis and the total current is the summation over all bands. Plugging 3.17 into 2.13 and 2.14, the current density

for right going carriers is found to be

$$J_{x,\eta,s_z}^{\rightarrow} = \frac{e}{(2\pi)^2} \int_{-\pi/2}^{\pi/2} d\theta \cos(\theta) \int_0^{\infty} k dk \frac{\hbar k v_f^2}{\sqrt{\hbar^2 k^2 v_f^2 + (-\eta s_z e E_z \ell + \lambda_{so})^2}} \left(\frac{1}{1 + e^{\frac{E(k)}{k_B T} - \eta_{\rightarrow}}} \right), \quad (4.11)$$

in which polar coordinates have been used and the angular component is integrated only over the right-going states. Converting to a dimensionless $u = E/k_B T$ space, the following current density relation is found

$$J_{x,\eta,s_z}^{\rightarrow} = \frac{e k_b^2 T^2}{4\pi^2 \hbar^2 v_f} \int_{\beta E_{CB}}^{\infty} du \sqrt{u^2 - \beta^2 (-\eta s_z e E_z \ell + \lambda_{so})^2} \left(\frac{1}{1 + e^{u - \eta_{\rightarrow}}} \right), \quad (4.12)$$

in which $\beta = 1/k_B T$. Since the only difference between the right-going and left-going carrier is the Fermi level, the total current is found to be

$$J_{x,\eta,s_z} = \frac{e k_b^2 T^2}{4\pi^2 \hbar^2 v_f} \int_{\beta E_{CB}}^{\infty} du \sqrt{u^2 - \beta^2 (-\eta s_z e E_z \ell + \lambda_{so})^2} \left(\frac{1}{1 + e^{u - \eta_{\rightarrow}}} - \frac{1}{1 + e^{u - \eta_{\leftarrow}}}} \right), \quad (4.13)$$

$$J_x^{Total} = \sum_{\eta} \sum_{s_z} J_{\eta,s_z} = 2(J_{x,+, \uparrow} + J_{x,+, \downarrow}), \quad (4.14)$$

where equation 4.13 is the total current density per conduction band and equation 4.14 is total current density over all conduction bands. As before, this "Fermi-Dirac-type" integral is not analytically solvable and therefore the current density is found computationally.

The current density at various symmetric and asymmetric gate voltages can be seen in figure 4.4. Regardless of the gate voltage symmetry, all plots eventually reach a saturation current density. As discussed in section 2.5, this saturation is expected and in the ballistic regime is due to the carriers being completely converted to right-going carriers. If we compare symmetric and asymmetric gate voltages, we see that the voltage required to achieve a certain saturation current is lower for the symmetric case since both gates are injecting carrier into the channel.

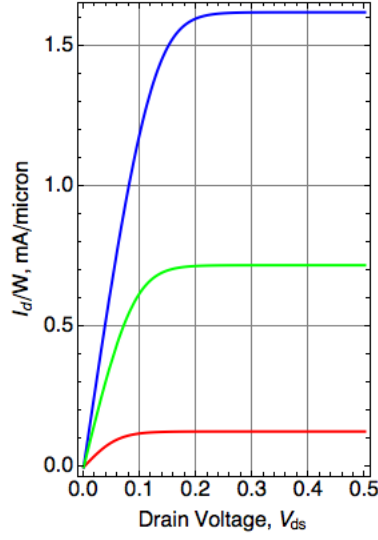


Figure 4.4: Current density at 300K and $V_{gs,TG} = V_{gs,BG} = 0$ V (red), $V_{gs,TG} = V_{gs,BG} = 0.2$ V (blue), and $V_{gs,TG} = 0.2$ V, $V_{gs,BG} = 0$ V (green)

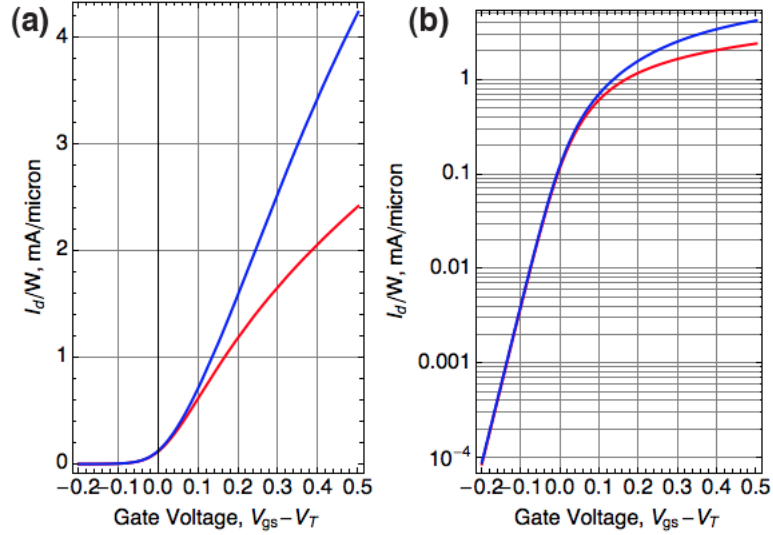


Figure 4.5: Current density at 300K and $V_{ds} = 0.1$ V (red) and $V_{ds} = 0.2$ V (blue) with symmetric gate voltages

In order to examine the subthreshold characteristics, looking at the dependence of current density on gate voltage is useful. Figure 4.5 shows the relationship between current density and symmetric gate voltage at various drain voltages. One can see that a subthreshold slope is produced regardless of drain voltage. Increasing the drain voltage effects the ON state by increasing

the current density ON/OFF ratio.

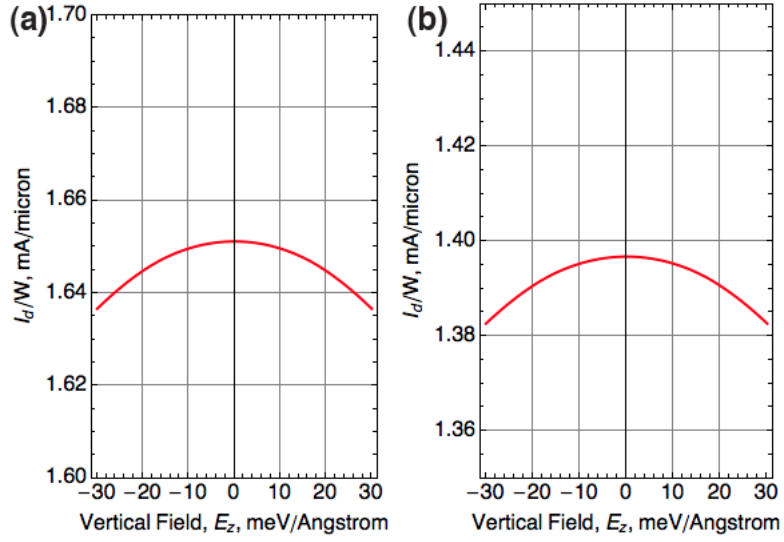


Figure 4.6: Current density at 300K and a) $E_f = 0.1$ eV and b) $ns = 5 \times 10^{12} \text{ cm}^{-2}$

Another useful property worth examining is the effect on the current density due to the channel's exposure to an electric field. By varying the gate voltages in such a way as to hold the carrier density or Fermi level constant, the vertical field in the channel can be independently adjusted. As shown in figure 4.6, the current does vary due to the electric field breaking spin degeneracy and shifting the conduction band edges, but the variations are quite small. As will be seen in the next section, the electric field has a far greater effect on the transverse current.

It should be noted that due to the symmetry of the bands the total source drain spin current, $J_{spin} = J_{\uparrow} - J_{\downarrow}$, is always zero. Again, we will find that this is not true for the transverse current. Furthermore, it should also be noted that this model is for electron transport, which is the why the current remains in an OFF state regardless of how negative the gate voltages become in figure 4.5. As seen in figure 4.7 and experimentally shown by Tao [10], once the gate voltages are

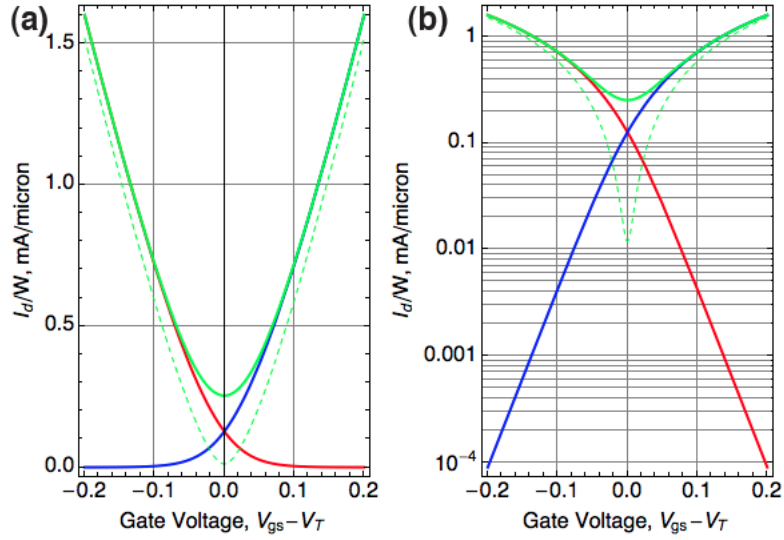


Figure 4.7: Current density at 300K (solid) and 50K (dashed) at $V_{ds} = 0.2$ V for electron transport (blue), hole transport (red), and total transport (green). Symmetric gate voltages are used.

low enough hole transport should take over and the current should rise. Consequently, if hole transport is included, the total current density never reaches a complete OFF state due to the insufficient band gap. The hole current density shown in figure 4.7 was found by taking advantage of the symmetry between the valence and conduction bands. However, if this symmetry was not present, the method previously described for electron transport could be applied to hole transport with only minor modifications. In order to reach a complete OFF state in silicene, one could either operate at a lower temperature, as shown in figure 4.7.

As shown in figure 4.8, looking at I_{ON}/I_{OFF} ratio is a more elucidating way to illustrate the effects of temperature on the switching capabilities of a FET. As the temperature decreases, the I_{ON}/I_{OFF} ratio increases, which is attributable to carriers being frozen out of the conduction and valence bands at lower temperatures. This behavior clearly demonstrates the increased switching capability of

the silicene FET at lower temperatures. Also, as expected, increasing the gate voltages also increases the I_{ON}/I_{OFF} ratio due to the increased amount of carriers injected into the channel. Overall, the standard source-drain characteristics of this silicene IDGFET are similar to that of a traditional FET.

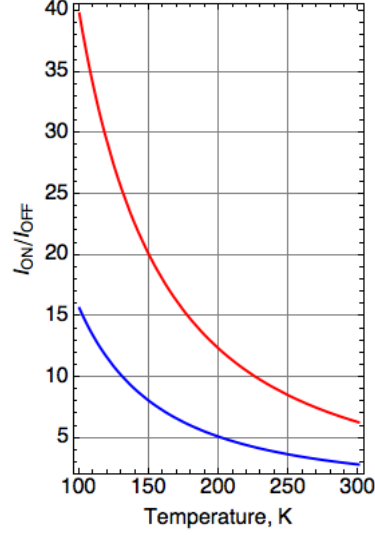


Figure 4.8: I_{ON}/I_{OFF} ratio at $V_{ds} = 0.2$ V, $V_{gs,TG}^{ON} = V_{gs,BG}^{ON} = 0.1$ V (blue), and $V_{gs,TG}^{ON} = V_{gs,BG}^{ON} = 0.2$ V (red).

4.3 Transverse Current

Due to the non-trivial Berry curvature, silicene will have a current component which is transverse to the traditional source-drain current. Similar to the previous section, the conduction band transverse current can be found by plugging the y direction velocities (equations 3.17 and 3.18) into equations 2.13-2.15. There are two components to this y direction current: the traditional group velocity current due to an applied voltage in the current direction and the current due to Berry curvature. Since there is no voltage applied across the channel in the y direction, there will be an equal amount of carriers going in the positive

and negative y direction and the total standard group velocity current will be zero. Therefore, the transverse current is solely a result of silicene's Berry curvature.

Plugging the Berry curvature velocity expression,

$$v_{yBerry,\eta,s_z} = -\frac{\eta e E_x \hbar v_f^2 (e E_z \ell - \eta s_z \lambda_{SO})}{2(\hbar^2 k^2 v_f^2 + (-\eta s_z e E_z \ell + \lambda_{SO})^2)^{3/2}} \hat{y}, \quad (3.19)$$

into the ballistic current equation, the following current density relation is found,

$$J_{Berry,\eta,s_z} = \frac{1}{(2\pi)^2} \int_0^{2\pi} d\theta \int_0^\infty k dk \frac{-e^2 \eta E_x \hbar v_f^2 (e E_z \ell - \eta s_z \lambda_{SO})}{2(\hbar^2 k^2 v_f^2 + (-\eta s_z e E_z \ell + \lambda_{SO})^2)^{3/2}} \frac{1}{1 + e^{\beta E(k) - \eta}}, \quad (4.15)$$

where $E_x = V_{ds} L_{ch}$ is the x direction electric field due to the drain bias. This assumes a linear voltage drop across the channel with t_{ch} being the channel length.

Changing to a dimensionless $u = E/k_B T$ space, the relationship becomes

$$J_{Berry,\eta,s_z} = \frac{-e^2 \eta E_x (e E_z \ell - \eta s_z \lambda_{SO})}{4\pi \hbar k_b T} \int_{\beta E_{CB}}^\infty \frac{u^{-2}}{1 + e^{u - \eta}}, \quad (4.16)$$

$$J_y^{total} = \sum_\eta \sum_{s_z} J_{Berry,\eta,s_z}, \quad (4.17)$$

$$J_y^{spin} = \sum_\eta J_{Berry,\eta,\uparrow} - \sum_\eta J_{Berry,\eta,\downarrow}, \quad (4.18)$$

where equation 4.17 is the total charge current and equation 4.18 is the total spin current.

Using the previously found source injection Fermi level, the Berry curvature current density can be solved computationally. Figure 4.9a shows the transverse current for one band (refer to appendix B for remaining bands) as well as the total transverse spin current at various gate voltages. One can clearly see that there is a current switching effect that occurs. This switching occurs when the vertical electric field in the channel crosses the critical value E_c . The current

directional switch occurs at $+E_c$ for the $K_{+,\uparrow}$ and $K_{-,\downarrow}$ bands and $-E_c$ for the $K_{+,\downarrow}$ and $K_{-,\uparrow}$ bands. However, when crossing either the positive or negative critical field, the direction to which the current densities of the two bands switch are opposite. Therefore, the total charge current is zero, because the current density of each band is always cancelled by another band with a current density of equal magnitude and opposite direction.

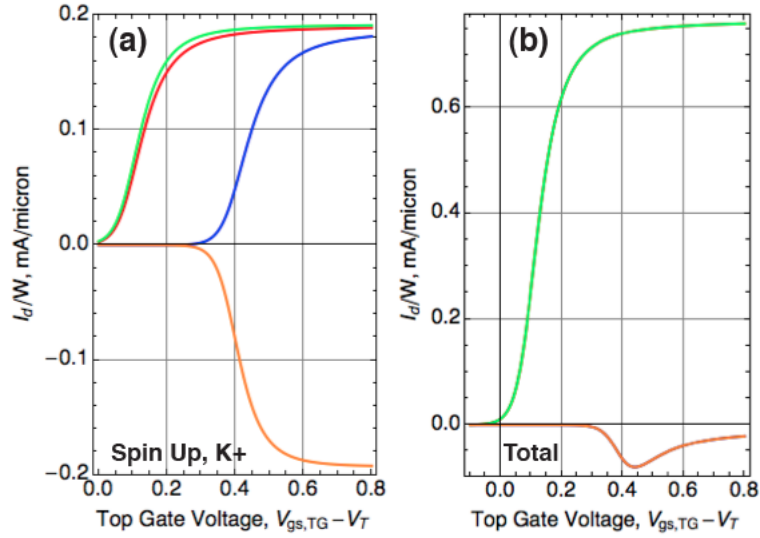


Figure 4.9: Transverse current density at 300K and $E_z = -5$ (red), $E_z = -20$ (blue), $E_z = 5$ (green), and $E_z = 20$ (orange). The left plot (a) is the current for spin up states near K_+ and the right plot (b) is the total spin current over all conduction bands. E_z in mV/Å.

As seen in figure 4.9b, the transverse spin current is not zero and also displays a unique switching effect. When $|E_z| < |E_c|$ there is a strong positive total spin current. When $|E_z| > |E_c|$, the total spin current switches direction and also becomes much smaller in magnitude.

To better characterize the effect that E_z has on the transverse spin current, figure 4.10 shows a plot of the spin current versus vertical field strength at various Fermi levels. The curves in figure 4.10 clearly show the strong switching behavior when the vertical field is swept through $|E_c|$.

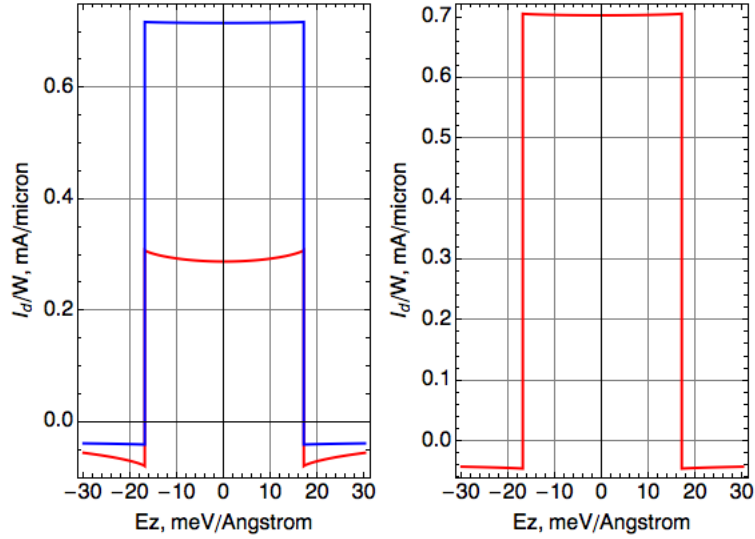


Figure 4.10: Total transverse spin current density at 300K at a) $E_f = 0$ eV (red) and $E_f = 0.1$ eV (blue) and b) $n_s = 5 \times 10^{12} \text{ cm}^{-2}$.

Just as with the source-drain current, it must be noted that the transverse current analysis up to this point is solely for conduction band electron transport. In order to capture the full picture, valence band hole transport must also be considered. The valence band Berry curvature of silicene is anti-symmetric to that of the conduction band (unaltered magnitude, but opposite sign). Therefore, due to this as well as the band structure symmetry, total valence band hole transport will also be anti-symmetric, as shown in figure 4.11a.

As shown in figure 4.11b, summing the conduction and valence band transport profiles gives the complete transport picture for the transverse spin current. Rather than going to zero as the gate bias becomes negative, the current density crosses zero at the point of gate antisymmetry and changes sign. The point of gate antisymmetry is the point at which the electron and hole current completely cancel each other. One can see that the switching between a HIGH and LOW state still occurs, but the form is now antisymmetric about the x axis.

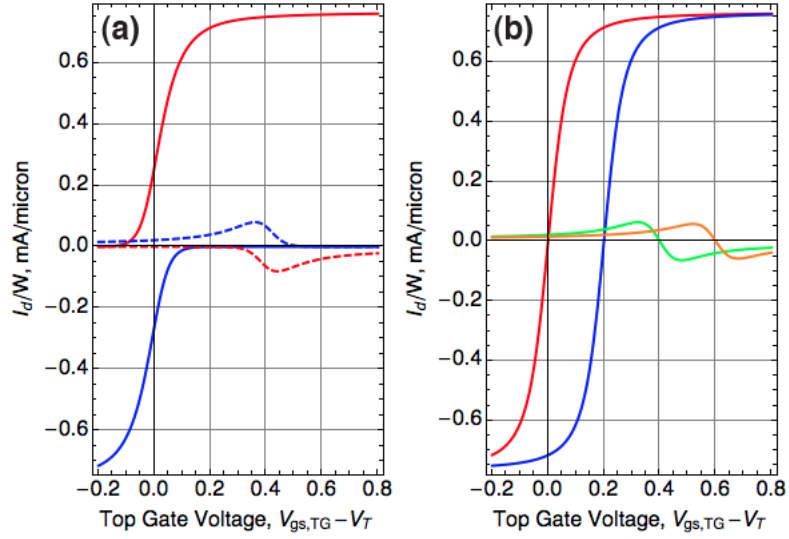


Figure 4.11: Transverse spin current density at 300K due to conduction and valence band transport. (a) Conduction (red) and valence (blue) band current densities at $E_z = 0$ (solid) and $E_z = 20$ (dashed). (b) Total current density at $E_z = 0$ (red), $E_z = 10$ (blue), $E_z = 20$ (green), and $E_z = 30$ (orange). E_z in mV/Å.

Since the spin current is reduced when $|E_z| > |E_c|$, this point of topological phase transition can also be thought of as a switch for turning the transverse spin current HIGH and LOW. However, it should be noted that the terms HIGH and LOW are only relative to each other.

As seen in figure 4.11a, when the transverse spin current is HIGH the spin current magnitude is comparable to the standard drain current. In the LOW state the magnitude is reduced, but is still very large relative to reported experimental values [29]. The spin current ratio is useful for comparing charge drain current to transverse spin current. The spin current ratio is defined as $\theta_{SH} = |J_s/J_c|$, where J_c is the charge drain current density and J_s is the spin current density. As seen in work by Dan Ralph [29], some of the highest values that have been reported are in the range of $\theta_{SH} = 0.12$ to 0.15 . However, as seen in figure 4.12, the spin current ratio for silicene is found to reach a maximum of ~ 1.15

at $L_{ch} = 10$ nm. Since the charge drain current density does not depend on channel length in the ballistic regime, the ratio can be tuned higher if the channel length is reduced. Even in the LOW state, the spin current ratio is found to be comparable to experimental values. More theoretical and experimental analysis is needed to determine the accuracy of these results, but this large spin current magnitude and the switching capability makes silicene potentially useful for spintronic devices.

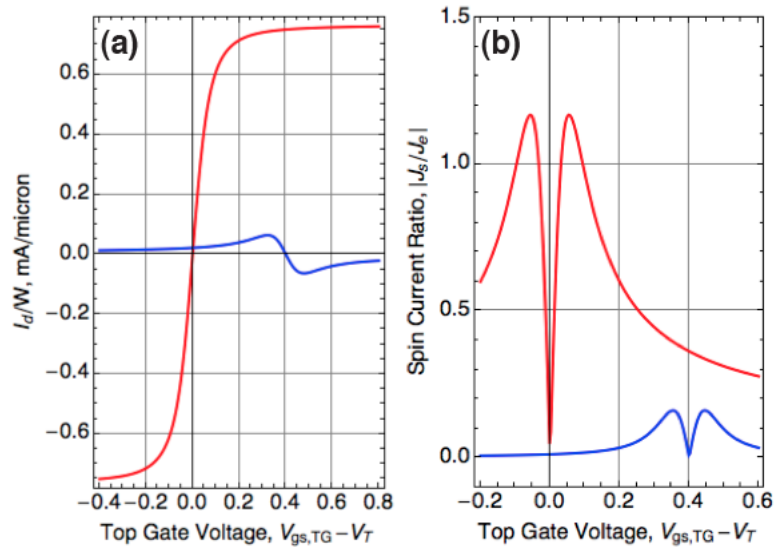


Figure 4.12: Spin current ratio at 300K, $V_{ds} = 0.1$ V, and $L_{ch} = 10$ nm. (a) Total spin current density at $E_z = 0$ mV/Å (red) and $E_z = 20$ mV/Å (blue). (b) Corresponding spin current ratios.

CHAPTER 5

CONCLUSIONS & FUTURE PROSPECTS

Silicene is a new 2D material that can be considered a silicon analog of graphene. Due to the buckled structure, silicene has been predicted to have numerous unique electronic and topological properties. In this thesis the material and device physics of silicene was examined in the ballistic transport regime. When exposed to an electric field perpendicular to the silicene plane, it was found that many unique properties do arise and can be adjusted via the electric field strength. Using a four-band low energy tight binding model, it was confirmed that a vertical electric field breaks spin degeneracy and causes two of the bands to become gapless at the critical field $|E_c|$. Furthermore, it was also confirmed that sweeping E_z through $|E_c|$ causes silicene to transition from topological insulator to band insulator.

The transport properties of silicene were also investigated by modeling a silicene channel independent double gate field effect transistor. It was found that the drain current exhibits the current saturation and the gate controlled carrier density that one expects in a standard FET. However, due to the non-trivial Berry curvature in silicene, there is a strong transverse velocity component. This velocity component leads to a spin current perpendicular to the drain current. It was shown that this spin current is largely switched to a HIGH state when the vertical field, which is dictated by the independent gate voltages, is less than the critical field value. When the field is larger than the critical value, the spin current switches direction, but also becomes relatively small and can be said to switch to a LOW state. This spin current switching is a very unique device property and could have potential applications in spintronics.

In an effort to further expand upon this work, there are some notable possibilities worth mentioning. Including the Rashba SOC component would prevent analytical solutions, but it would provide greater accuracy. There has also been research done into the properties of silicene in the presence of a magnetic field and it seems as though this field combined with the vertical electric field can lead to more unique properties, such as the quantum anomalous hall state [30, 31]. Examining the transport properties in this regime could lead to more new device applications. However, the ultimate goal of this research should be to actually attempt to grow silicene devices and test them for these unique and interesting properties.

APPENDIX A

ELECTRON VELOCITY PROFILES

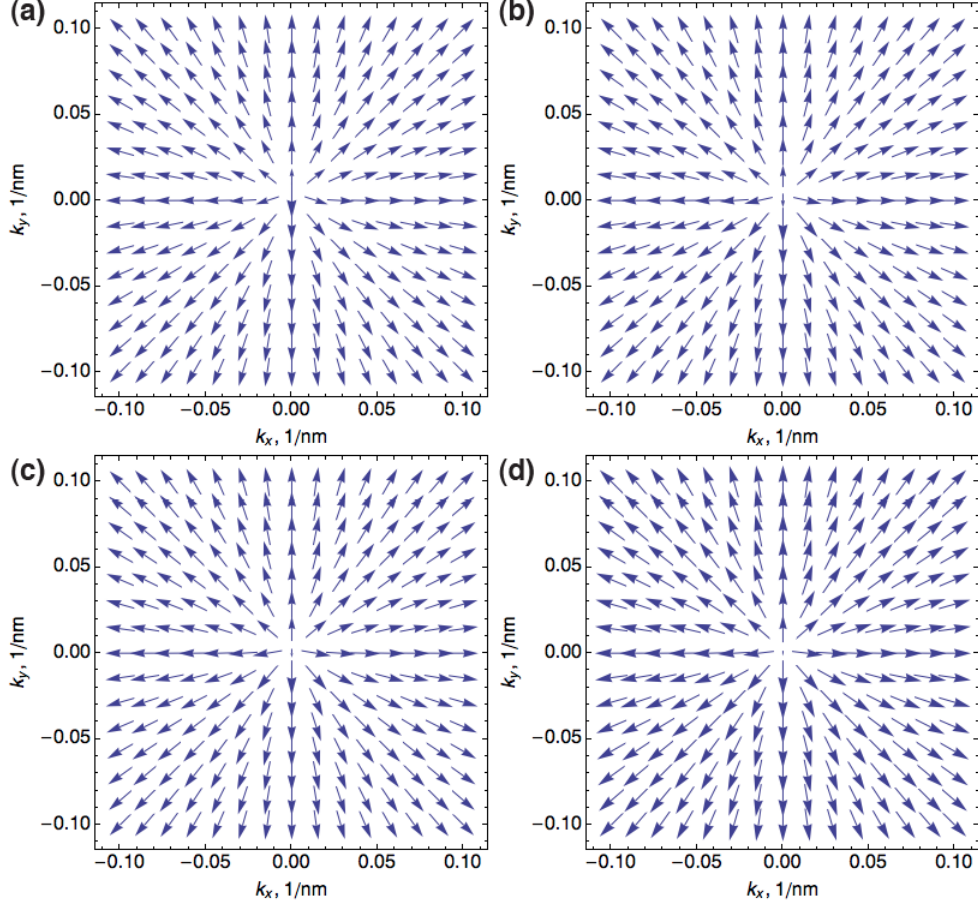


Figure A.1: Spin down conduction band velocity profile near K_+ Dirac point at a) $E_z = 0$, b) $E_z < E_c$, $E_z > E_c$, and d) $E_z \gg E_c$. The length of the arrows are proportional to the magnitude of the velocities.

For a vertical electric field sweeping through E_c in the positive direction, figure A.1 shows the velocity profile of spin down states near the K_+ Dirac point. The velocity profiles of spin up and down states near the K_- Dirac point are shown in figures A.2 and A.3. The velocities of the spin up states near K_+ and spin down states near K_- switch direction when E_z is swept through E_c in the positive direction. In the negative direction, the opposite states will be the ones to switch direction.

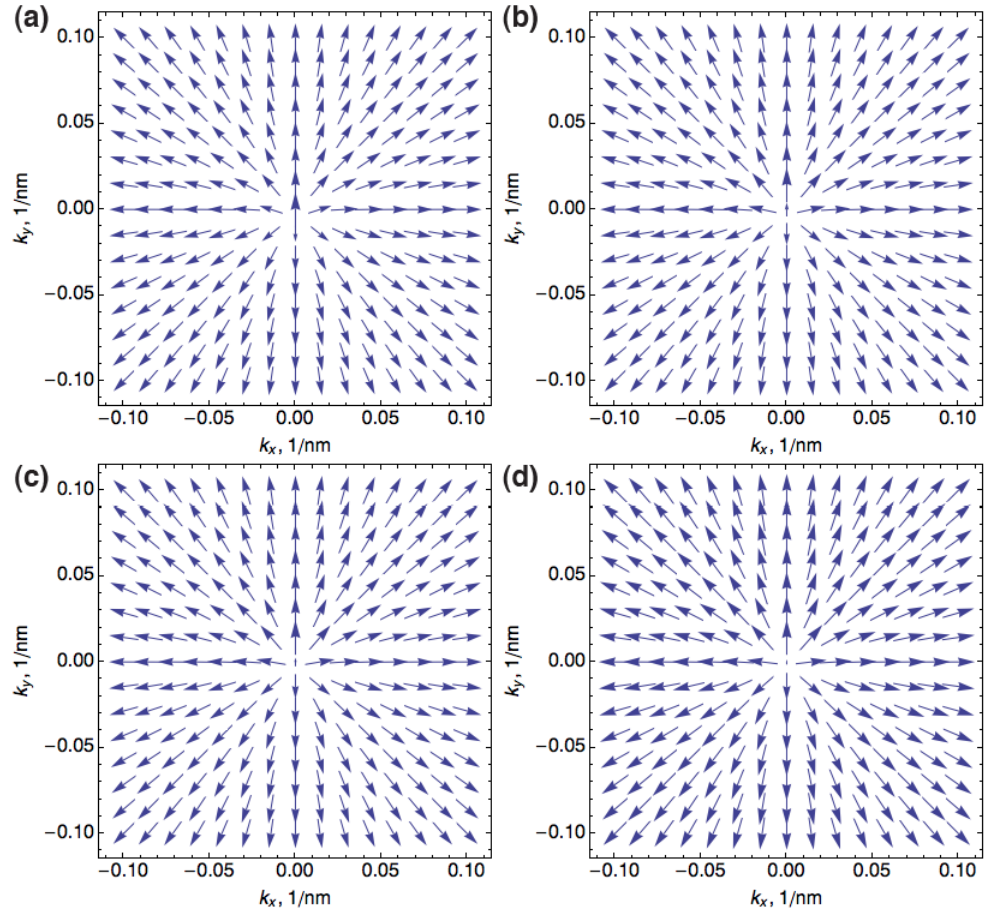


Figure A.2: Spin up conduction band velocity profile near K -Dirac point at a) $E_z = 0$, b) $E_z < E_c$, $E_z > E_c$, and d) $E_z \gg E_c$. The length of the arrows are proportional to the magnitude of the velocities.

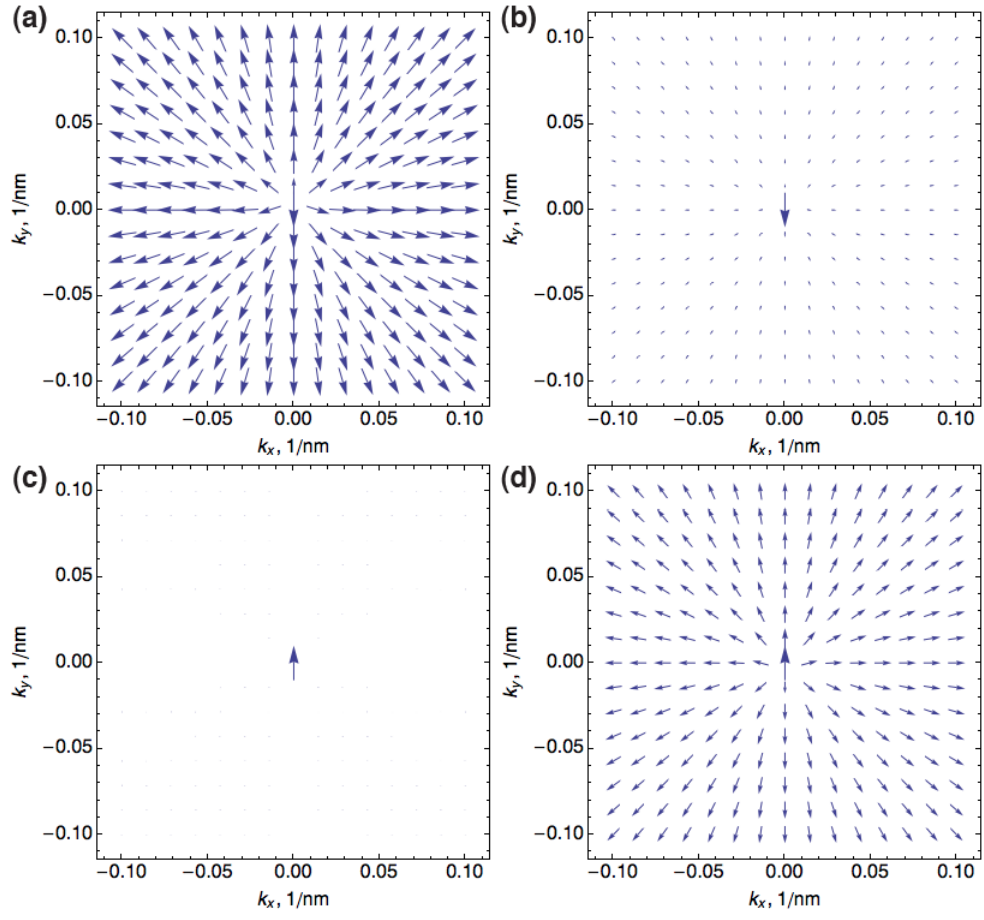


Figure A.3: Spin down conduction band velocity profile near K_- Dirac point at a) $E_z = 0$, b) $E_z < E_c$, $E_z > E_c$, and d) $E_z \gg E_c$. The length of the arrows are proportional to the magnitude of the velocities.

APPENDIX B

TRANSVERSE ELECTRON CURRENT

The silicene IDGFET transverse spin current contributions from the remaining conduction bands is shown in figure B.1.

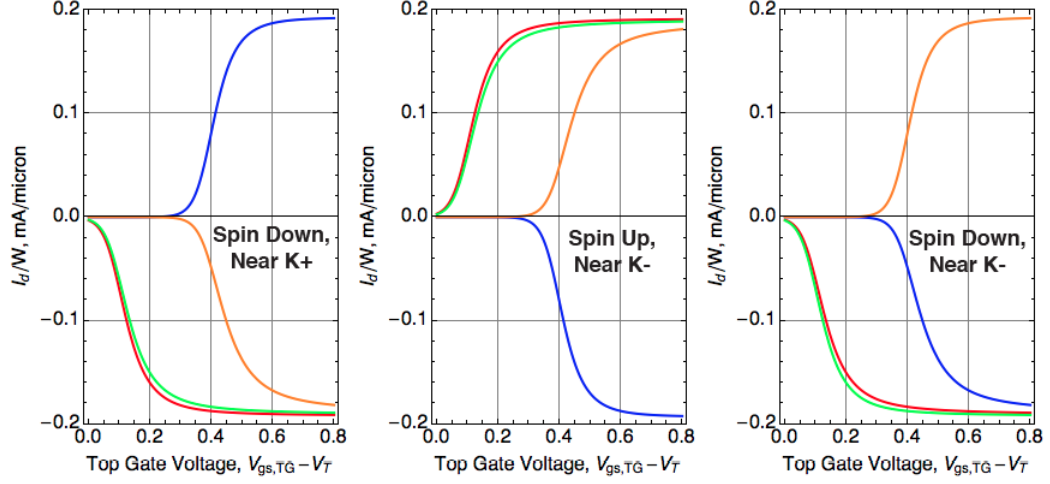


Figure B.1: Transverse spin current at 300K and $E_z = -5$ (red), $E_z = -20$ (blue), $E_z = 5$ (green), and $E_z = 20$ (orange). E_z in mV/Å.

BIBLIOGRAPHY

- [1] J. Bardeen and W. H. Brattain, "The Transistor, a Semi-Conductor Triode," *Physical Review*, pp. 1–2, 1948.
- [2] D. Jena, "Tunneling transistors based on graphene and 2-D Crystals," *Proceedings of the IEEE*, vol. 101, no. 7, pp. 1585–1602, 2013.
- [3] A. F. K.S. Novoselov, A.K. Geim, S.V. Morozov, D. Jiang, Y. Zhang, S.V. Dubonos, I.V. Grigorieva, "Electric Field Effect in Atomically Thin Carbon Films," *Science*, vol. 306, no. 5696, pp. 666–669, 2004.
- [4] A. H. Castro Neto, F. Guinea, N. M. R. Peres, K. S. Novoselov, and A. K. Geim, "The electronic properties of graphene," *Reviews of Modern Physics*, vol. 81, no. 1, pp. 109–162, 2009.
- [5] M. O. Goerbig, "Electronic properties of graphene in a strong magnetic field," *Reviews of Modern Physics*, vol. 83, no. 4, 2011.
- [6] C. Bena and G. M. Baux, "Remarks on the tight-binding model of graphene," *New Journal of Physics*, vol. 11, 2009.
- [7] K. Majumdar, K. V. R. M. Murali, N. Bhat, and Y. M. Lin, "Intrinsic limits of subthreshold slope in biased bilayer graphene transistor," *Applied Physics Letters*, vol. 96, no. 12, pp. 3–5, 2010.
- [8] X. Xu, "Spin and pseudospins in transition metal dichalcogenides," *Proceedings - 2014 Summer Topicals Meeting Series, SUM 2014*, vol. 10, no. May, pp. 1–2, 2014.
- [9] M. Ezawa, "A topological insulator and helical zero mode in silicene under an inhomogeneous electric field," *New Journal of Physics*, vol. 14, 2012.
- [10] L. Tao, E. Cinquanta, D. Chiappe, C. Grazianetti, M. Fanciulli, M. Dubey, A. Molle, and D. Akinwande, "Silicene field-effect transistors operating at room temperature.," *Nature nanotechnology*, vol. 10, no. February, pp. 1–5, 2015.
- [11] S. Konschuh, M. Gmitra, and J. Fabian, "Tight-binding theory of the spin-orbit coupling in graphene," *Physical Review B*, vol. 82, no. 24, p. 245412, 2010.

- [12] R. Winkler, *Spin Orbit Coupling Effects in Two-Dimensional Electron and Hole Systems*. 2003.
- [13] C. L. Kane and E. J. Mele, "Quantum Spin hall effect in graphene," *Physical Review Letters*, vol. 95, no. 22, pp. 1–4, 2005.
- [14] D. Xiao, M. C. Chang, and Q. Niu, "Berry phase effects on electronic properties," *Reviews of Modern Physics*, vol. 82, no. 3, pp. 1959–2007, 2010.
- [15] M. Berry, "Quantal phase factors accompanying adiabatic changes," 1984.
- [16] K. V. Klitzing, G. Dorda, and M. Pepper, "New method for high-accuracy determination of the fine-structure constant based on quantized hall resistance," *Physical Review Letters*, vol. 45, no. 6, pp. 494–497, 1980.
- [17] D. J. Thouless, M. Kohmoto, M. P. Nightingale, and M. Den Nijs, "Quantized hall conductance in a two-Dimensional periodic potential," *Physical Review Letters*, vol. 49, no. 6, pp. 405–408, 1982.
- [18] M. Z. Hasan and C. L. Kane, "Colloquium: Topological insulators," *Reviews of Modern Physics*, vol. 82, no. 4, pp. 3045–3067, 2010.
- [19] C. L. Kane and E. J. Mele, "Z₂ topological order and the quantum spin hall effect," *Physical Review Letters*, vol. 95, no. 14, pp. 3–6, 2005.
- [20] M. König, S. Wiedmann, C. Brüne, A. Roth, H. Buhmann, L. W. Molenkamp, X.-l. Qi, and S.-c. Zhang, "in HgTe Quantum Wells," *Science*, vol. 318, no. November, pp. 766–771, 2007.
- [21] J. E. Moore, "The birth of topological insulators.," *Nature*, vol. 464, no. 7286, pp. 194–8, 2010.
- [22] L. a. Jauregui, M. T. Pettes, L. P. Rokhinson, L. Shi, and Y. P. Chen, "Gate tunable relativistic mass and Berry's phase in topological insulator nanoribbon field effect devices.," *Scientific reports*, vol. 5, p. 8452, 2015.
- [23] X. L. Qi and S. C. Zhang, "Topological insulators and superconductors," *Reviews of Modern Physics*, vol. 83, no. 4, 2011.
- [24] D. N. Sheng, Z. Y. Weng, L. Sheng, and F. D. M. Haldane, "Quantum spin-hall effect and topologically invariant chern numbers," *Physical Review Letters*, vol. 97, no. 3, pp. 1–4, 2006.

- [25] A. Roth, C. Brüne, H. Buhmann, L. W. Molenkamp, J. Maciejko, X.-L. Qi, and S.-C. Zhang, “Nonlocal transport in the quantum spin Hall state,” *Science (New York, N.Y.)*, vol. 325, no. 5938, pp. 294–7, 2009.
- [26] K. Natori, “Ballistic metal-oxide-semiconductor field effect transistor,” *Journal of Applied Physics*, vol. 76, no. 8, pp. 4879–4890, 1994.
- [27] D. Jena, “Physics of Semiconductors: Notes, Cornell University,” p. 30, 2016.
- [28] C. C. Liu, H. Jiang, and Y. Yao, “Low-energy effective Hamiltonian involving spin-orbit coupling in silicene and two-dimensional germanium and tin,” *Physical Review B - Condensed Matter and Materials Physics*, vol. 84, no. 19, pp. 1–11, 2011.
- [29] L. Liu, C.-F. Pai, Y. Li, H. W. Tseng, D. C. Ralph, and R. A. Buhrman, “Spin-Torque Switching with the Giant Spin Hall Effect of Tantalum,” *Science*, vol. 336, no. 6081, pp. 555–558, 2012.
- [30] M. Ezawa, “Valley-polarized metals and quantum anomalous hall effect in silicene,” *Physical Review Letters*, vol. 109, no. 5, pp. 1–5, 2012.
- [31] V. Vargiamidis and P. Vasilopoulos, “Electric- and exchange-field controlled transport through silicene barriers: Conductance gap and near-perfect spin polarization,” *Applied Physics Letters*, vol. 105, no. 22, pp. 1–5, 2014.